Journal of Sound and Vibration (2002) **254**(2), 327–366
doi:10.1006/jsvi.2001.4116, available online at http://www.idealibrary.com on IDEAL®

IDENTIFICATION OF MULTIPLE FAULTS IN ROTOR SYSTEMS

N. Bachschmid, P. Pennacchi and A. Vania

Dipartimento di Meccanica, Politecnico di Milano, Via La Masa, 34, *I*-20158 *Milano, Italy*.
E-mail: *nicolo.bachschmid@polimi.it*; *paolo.pennacchi@polimi.it*; *andrea.vania@polimi.it*

(*Received* 8 *May* 2001, *and in final form* 16 *October* 2001)

Many papers are available in the literature about identification of faults in rotor systems. However, they generally deal only with a single fault, usually an unbalance. Instead, in real machines, the case of multiple faults is quite common: the simultaneous presence of a bow (due to several different causes) and an unbalance or a coupling misalignment occurs often in rotor systems. In this paper, a model-based identification method for multiple faults is presented. The method requires the definition of the models of the elements that compose the system, i.e., the rotor, the bearings and the foundation, as well as the models of the faults, which can be represented by harmonic components of equivalent force or moment systems. The identification of multiple faults is made by a least-squares fitting approach in the frequency domain, by means of the minimization of a multi-dimensional residual between the vibrations in some measuring planes on the machine and the calculated vibrations due to the acting faults. Some numerical applications are reported for two simultaneous faults and some experimental results obtained on a test-rig are used to validate the identification procedure. The accuracy and limits of the proposed procedure have been evaluated.

1. INTRODUCTION

In past few years several papers about fault identification have appeared in the literature, dealing with many application fields and introducing different methods. A rather complete survey with a rich bibliography, which ranges in the last 20 years, is reported in reference [1]. The identification procedure can be performed as usual by means of causality correlations of measurable symptoms to the faults. As regards the rotordynamics field and limiting to the most recent contributes, two main approaches can be used.

In the first approach, the symptoms can be defined using qualitative information, based on human operators' experience, which creates a knowledge base. A recent contribution is given in reference [2]: an expert system can be built up in which different diagnostic reasoning strategies can be applied. Fault-symptom matrices, fault-symptom trees, if–then rules or fuzzy logic classifications can be used to indicate in a probabilistic approach the type, and sometimes also the size and the location of the most probable fault. Also artificial neural networks (ANN) can be used for creating the symptom-fault correlation. This qualitative diagnostic approach is widely used both in industrial environments and in advanced research work.

The second approach is quantitative and is called the model-based fault detection method. In this case, a reliable model of the system or of the process is used for creating the symptom-fault correlation, or the input–output relation. However, this method has many different ways of application. Among recent contributions available in the literature, Mayes

0022-460X/02/$35.00

and Penny [3] introduce a fuzzy clustering method in which the basis is to consider the vibration data as a high-dimension feature vector and the vibration caused by a particular fault on a specific machine can considered to be a point in this high-dimension space. This same fault, on a number of similar machine, should produce a cluster of points in the high-dimension space that is distinct from other clusters produced by different faults. The main drawback of this method is the availability of a large database of the dynamic behaviour of similar machines, which can emphasize the differences in the response of similar machines.

In other applications, the fault detection can be performed by means of different model-based approaches, according to the nature of the system under observation:

- parameter estimation, when the characteristic constant parameters of the process, or of the components are affected by the fault.
- state estimation, when the constant parameters are unaffected by possible faults and only the state of the system, which is represented by a set of generally unmeasurable state variables (function of time), is affected by the faults; in this case the model acts as a state observer.
- parity equations, when the faults affect some of the unmeasurable input variables, the parameters are constant, and only output variables are measured and compared with calculated model output variables.

Therefore, the fault can be identified from parameter or state estimation or from parity equations.

Kreuzinger-Janik and Irretier [4] use a modal expansion of the frequency response function of the system, on both numerical model and experimental results, to identify the unbalance distribution of a rotor. Markert *et al.* [5] and Platz *et al.* [6] present a model in which equivalent loads due to the faults (rubbing and unbalances) are virtual forces and moments acting on the linear undamged system model to generate a dynamic behaviour are identical to the measured one of the damaged system. The identification is then performed by least-squares fitting in the time domain. Edwards *et al.* [7] employ a model-based identification in the frequency domain to identify an unbalance on a test-rig.

A more comprehensive approach, able to identify several different types of faults and to discriminate among faults which generate similar harmonic components, has been introduced by Bachschmid and Pennacchi [8]. This method has been experimentally validated on different test-rigs and real machines (see also references [9–12]) for many types of faults, such as unbalances, rotor permanent bows, rotor rubs, coupling misalignments, cracks, journal ovalization and rotor stiffness asymmetries. In this model-based identification procedure, the input variables are the exciting forces and the output variables are the vibrations. The procedure requires the model definition of the elements (rotors, bearings, supporting structure) that compose the rotor system. A finite beam element model is assumed for the rotor, the bearings are represented by means of their stiffness and damping matrices (therefore, non-linear oil film effects are neglected), while several representations can be given for the foundation, such as modal, elasto-dynamic matrix or lumped springs and dampers. Also, the effect of the faults has to be modelled and this is done by introducing an equivalent system of external forces and moments. In this paper, the method is improved in order to identify simultaneously two or more faults acting on a rotor, since the case of multiple faults may occur in real machines: sometimes a bow (due to several different causes) and an unbalance or a coupling misalignment may develop simultaneously.

Generally, the fault identification procedure is started when the vibration vector change exceeds a suitable pre-established acceptance region; in this case, it is more likely that the change in the vibrational behaviour is really caused by an impeding fault only. But when the

reference situation is not available, the arising fault is superposed to the original unbalance and bow distribution. In this case also, the multiple fault identification may be useful for selecting the simultaneous faults.

2. FAULT MODELLING

Before introducing the fault models and the identification procedure for multiple faults, it is necessary to introduce the reference systems used in the two-dimensional (2D) finite element (f.e.) model of the rotor. Each node of the model has four degrees of freedom (d.o.f.). If one considers the two subsequent nodes, the jth and the $j+1$th, they define the element jth, as shown in Figure 1.

Defining the vector $\mathbf{x}^{(j)}$ of the generalized displacements of the jth node as

$$\mathbf{x}^{(j)} = [x_j \;\; \vartheta_{x_j} \;\; y_j \;\; \vartheta_{y_j}]^{\mathrm{T}}, \tag{1}$$

the vector $\mathbf{x}$ of the generalized displacements of all the nodes of the rotor is composed of all the ordered vectors $\mathbf{x}^{(j)}$:

$$\mathbf{x} = [\cdots \quad x_j \;\; \vartheta_{x_j} \;\; y_j \;\; \vartheta_{y_j} \;\; x_{j+1} \;\; \vartheta_{x_{j+1}} \;\; y_{j+1} \;\; \vartheta_{y_{j+1}} \quad \cdots]^{\mathrm{T}}. \tag{2}$$

Moreover, a rotating force $\mathbf{F}^{(k)}$ of amplitude $\mathbf{F}^{(k)}$ and phase $\varphi^{(k)}$, and a rotating moment $\mathbf{M}^{(k)}$ of amplitude $M^{(k)}$ and phase $\varphi^{(k)}$, with a frequency of $n\Omega$ acting on the jth node have the following representation:

$$\mathbf{F}^{(k)} = \left[0 \;\vdots\; \underbrace{1 \;\; 0 \;\; i \;\; 0}_{j\text{th node}} \;\vdots\; 0\right]^{\mathrm{T}} \cdot F^{(k)} \mathrm{e}^{\mathrm{i}\varphi^{(k)}} \mathrm{e}^{\mathrm{i}n\Omega t}, \tag{3}$$

$$\mathbf{M}^{(k)} = \left[0 \;\vdots\; \underbrace{0 \;\; 1 \;\; 0 \;\; i}_{j\text{th node}} \;\vdots\; 0\right]^{\mathrm{T}} \cdot M^{(k)} \mathrm{e}^{\mathrm{i}\varphi^{(k)}} \mathrm{e}^{\mathrm{i}n\Omega t}. \tag{4}$$

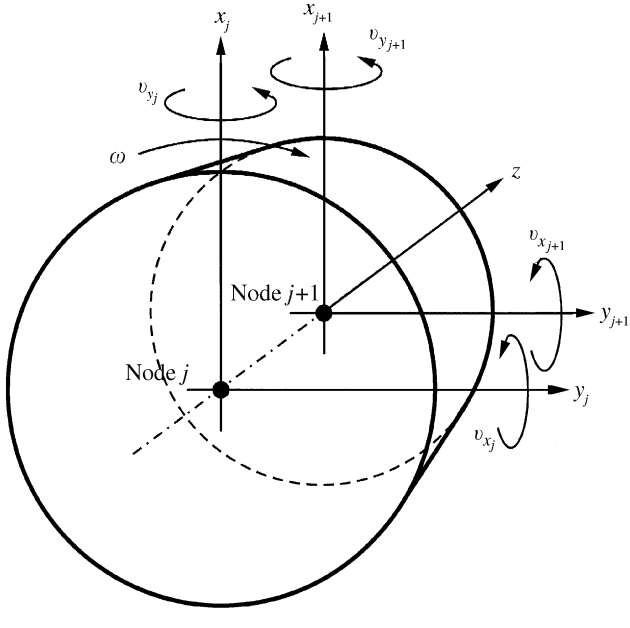

Figure 1. Reference system on a general rotor element j.

In the parameter estimation approach, the identification of the changes in the system parameters due to the fault seems to be a more difficult task than the identification of the equivalent external forces, because the system parameters influence generally the complete mass, stiffness and damping matrices of the system. In other words, with reference to the standard matrix equation of the system

$$\mathbf{M}\ddot{\mathbf{x}}_t + \mathbf{D}\dot{\mathbf{x}}_t + \mathbf{K}\mathbf{x}_t = \mathbf{F}(t), \tag{5}$$

it seems difficult to identify the changes in the matrices **M**, **D**, and **K** from measurement of vibration $\mathbf{x}_t$, in only a few measuring points along the shaft, such as those that occur in real machines. Now, indicate by d**M**, d**D** and d**K** the changes in mass, damping and stiffness matrices due to system parameter changes caused by the fault. Equation (5) yields

$$(\mathbf{M} + \mathrm{d}\mathbf{M})\ddot{\mathbf{x}}_t + (\mathbf{D} + \mathrm{d}\mathbf{D})\dot{\mathbf{x}}_t + (\mathbf{K} + \mathrm{d}\mathbf{K})\mathbf{x}_t = \mathbf{W} + (\mathbf{U} + \mathbf{M}_u)\mathrm{e}^{\mathrm{i}\Omega t}, \tag{6}$$

in which the right side external forces $\mathbf{F}(t)$ are generally unknown, because they are composed of the weight (which is known) and of the original unbalance and bow (which are unknown). If the system is considered to be linear, then the total vibration $\mathbf{x}_t$ can be considered to be split into two terms which can be simply superposed:

$$\mathbf{x}_t = \mathbf{x}_1 + \mathbf{x}. \tag{7}$$

The first vibration vector ($\mathbf{x}_1$) is due to the weight **W** as well as due to the unknown unbalance force $\mathbf{U}\mathrm{e}^{\mathrm{i}\Omega t}$ and unbalance moment $\mathbf{M}_u\mathrm{e}^{\mathrm{i}\Omega t}$, and the second term (**x**) is due to the fault. The component **x** may be obtained by calculating the vector differences of the actual vibrations (due to weight, original unbalance and fault) minus the original vibrations measured, in the same operating conditions (rotation speed, flow rate, power, temperature, etc.) before the fault occurrence. Recalling the definition of $\mathbf{x}_1$, the pre-fault vibration, following equation holds:

$$\mathbf{M}\ddot{\mathbf{x}}_1 + \mathbf{D}\dot{\mathbf{x}}_1 + \mathbf{K}\mathbf{x}_1 = \mathbf{W} + (\mathbf{U} + \mathbf{M}_u)\mathrm{e}^{\mathrm{i}\Omega t}, \tag{8}$$

which when substituted into equation (6) gives

$$\mathbf{M}\ddot{\mathbf{x}} + \mathbf{D}\dot{\mathbf{x}} + \mathbf{K}\mathbf{x} = -\mathrm{d}\mathbf{M}\ddot{\mathbf{x}}_t - \mathrm{d}\mathbf{D}\dot{\mathbf{x}}_t - \mathrm{d}\mathbf{K}\mathbf{x}_t. \tag{9}$$

The right side of equation (9) can be considered as a system of equivalent external forces, which force the fault-free system to have the change in vibrations defined by **x** that is due to the developing fault only:

$$\mathbf{M}\ddot{\mathbf{x}} + \mathbf{D}\dot{\mathbf{x}} + \mathbf{K}\mathbf{x} = \mathbf{F}_f(t). \tag{10}$$

Using this last approach, the problem of fault identification is then reduced to a force identification procedure with known system parameters, keeping in mind that a particular force system corresponds to each type of fault considered, as explained in the following. Since the final goal is the identification of faults, this approach is preferred since only a few elements of the unknown fault forcing vector are in reality different from zero, which reduces significantly the number of unknowns to be identified. In fact, the forces that model each fault are considered to be applied at not more than two different nodes along the rotor. If one considers a steady state situation, assuming linearity of the system and applying the harmonic balance criteria from equation (10), one gets, for each harmonic component, the equations

$$[-(n\Omega)^2\mathbf{M} + \mathrm{i}n\Omega\mathbf{D} + \mathbf{K}]\mathbf{X}_n = \mathbf{F}_{f_n}(\Omega), \tag{11}$$

where the force vector $\mathbf{F}_{f_n}$ has to be identified. This force vector could be a function of Ω or not depending on the type of the fault. It is worth stressing that if the presence of several

faults (for instance m faults) is considered, then the force vector $\mathbf{F}_{f_n}$ is composed of several vectors $\mathbf{F}_{f_n}^{(1)}, \mathbf{F}_{f_n}^{(2)}, \ldots, \mathbf{F}_{f_n}^{(m)}$:

$$\mathbf{F}_{f_n}(\Omega) = \sum_{i=1}^{m} \mathbf{F}_{f_n}^{(i)}(\Omega). \tag{12}$$

Few spectral components in the frequency domain (generally not more than three, in the absence of rolling bearings and gears) $\mathbf{X}_n$, measured in correspondence of the bearings, represent completely the periodical vibration time history.

Moreover, the kth fault acts on few d.o.f. of the system, so that the vector $\mathbf{F}_{f_n}^{(k)}$ is not a full-element vector which is convenient to be represented by

$$\mathbf{F}_{f_n}^{(k)}(\Omega) = [\mathbf{F}_L^{(k)}]\mathbf{A}^{(k)}(\Omega), \tag{13}$$

where $[\mathbf{F}_L^{(k)}]$ is the localization vector which has all null-elements except for the d.o.f. to which the forcing system is applied, see equations (3) and (4), and $\mathbf{A}^{(k)}(\Omega)$ is the complex vector of the identified defects. The vector $[\mathbf{F}_L^{(k)}]$ does not give just the assumed position of the defect but also expresses the link between the force fault system and the modulus and phase of the identified fault that produce it. Some fault models are examined in detail in the following sections.

2.1. UNBALANCE FAULT MODEL

The unbalance has only a $1x$ rev. component. The complex vector of the general kth fault force system $\mathbf{F}_{f_1}^{(k)}$ becomes in this case:

$$\mathbf{F}_{f_1}^{(k)} = [0 \;\vdots\; 1 \;\; 0 \;\; i \;\; 0 \;\vdots\; 0]^{\mathrm{T}} \cdot (mr)^{(k)} \Omega^2 \mathrm{e}^{\mathrm{i}\varphi^{(k)}} = [\mathbf{F}_L^{(k)}]\mathbf{A}^{(k)}(\Omega), \tag{14}$$

where the only elements different from zero are the ones relative to the horizontal and vertical d.o.f. of the node j, where the unbalance is supposed to be applied. Note that in this case the fault force system is function of the rotating speed Ω.

2.2. BOW AND RIGID COUPLING MISALIGNMENT FAULT MODELS

The thermal or permanent bow and the rigid coupling misalignment are analyzed together, because both faults generate an asymmetrical axial strain distribution which deflects the rotor.

In fact, a (rotating) thermal bow of a rotor is due to an asymmetrical heating or cooling of the symmetrical rotor, or due to an axial symmetry thermal distribution of an asymmetrical rotor, where both cause an asymmetrical axial strain distribution on the cross-section of the shaft. The asymmetrical heating can be localized when it is due to a full annular rub (local bow), or can be extended to a certain length of the rotor, as in a generator when a cooling duct is obstructed (extended bow). A similar asymmetrical strain distribution is caused by a radial or angular misalignment of a rigid coupling between two rotors of a shaft line. The rigid coupling misalignment can be due to manufacturing errors of the two surfaces of the flanges, assembling errors (different tightening forces in the connecting bolts) or corrosion. The strain distribution does not influence the system parameters and may be considered as created by an external system of forces, provided that the associated vibrations in the bearings are small enough to consider the system as linear.

The bow can be simulated, generally in a fairly accurate way, by imposing on the rotor, in only two nodes of the f.e. model, a suitable system of rotating bending moments, which generates the same (polarly asymmetrical) strains and therefore the same static deflection.

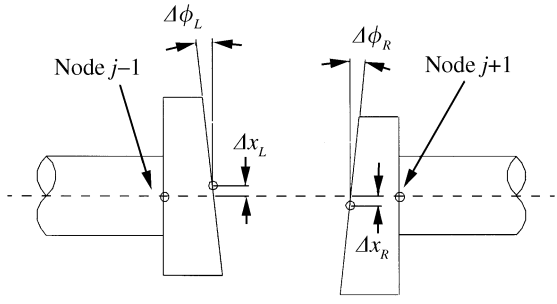

Figure 2. Representation of the angular and radial misalignment of the two flanges of the coupling.

Therefore, at each of the two nodes of the f.e. model (the extremity nodes of the part of the rotor which is interested by the bow), only one rotating moment is applied, in order to have an easier identification procedure.

A similar situation holds also for the coupling misalignment fault: this can be simulated by suitable rotating moments and forces. The nodes where the fault force system is applied are the extremity nodes of the flanges of the coupling where the misalignment occurs: also this malfunction can be considered as a local bow.

Therefore, for the identification procedure, both these faults are given by a rotating, speed-independent, force system that generates, statically, the deflection and, dynamically, at the operating speed, the total vibration of the shaft.

The complex vector of the fault force system $\mathbf{F}_{f_1}^{(k)}$, which simulates the kth bow, and the corresponding $[\mathbf{F}_L^{(k)}]$ and $\mathbf{A}^{(k)}$ become

$$\begin{aligned} [\mathbf{F}_L^{(k)}] &= [0 \,\vdots\, 0 \;\; i \;\; 0 \;\; 1 \,\vdots\, 0 \,\vdots\, 0 \;\; -i \;\; 0 \;\; -1 \,\vdots\, 0]^{\mathrm{T}}, \\ \mathbf{A}^{(k)} &= M^{(k)} \mathrm{e}^{\mathrm{i}\varphi^{(k)}}, \end{aligned} \tag{15}$$

where the only elements different from zero are the ones relative to the horizontal and vertical rotational d.o.f. of two nodes.

The rigid coupling misalignment is simulated by a balanced force system, independent of rotating speed, applied to the coupling flanges. This force system produces a deformation of the finite beam elements that simulate the coupling, which reproduces the angular and radical deflection of the nodes $(j-1)$ and $(j+1)$ of the flanges and makes the rotor assume the static deflection due to this defect (Figure 2).

The corresponding localization matrix $[\mathbf{F}_L^{(k)}]$ and the parameters vector $\mathbf{A}^{(k)}$ are, in case of angular and radial misalignment:

$$[\mathbf{F}_L^{(k)}] = [0 \;\; \cdots \;\; K_{R,j-1} \, K_{R,j+1} \;\; \cdots \;\; 0]^{\mathrm{T}} \cdot \begin{bmatrix} 1 & 0 \\ 0 & i \\ i & 0 \\ 0 & 1 \end{bmatrix}, \quad \mathbf{A}^{(k)} = \begin{bmatrix} \Delta\mathbf{x}_R^{(k)} + \Delta\mathbf{x}_L^{(k)} \\ \Delta\phi_R^{(k)} + \Delta\phi_L^{(k)} \end{bmatrix}, \tag{16}$$

where $K_{R,j-1}$ and $K_{R,j+1}$ are the stiffnesses of the rotor system reduced to the coupling extremity nodes.

2.3. TRANSVERSE CRACK AND AXIAL ASYMMETRY FAULT MODELS

It has been shown in literature [13] that a crack can be modelled by a suitable system of external forces or moments, which depend on the depth of the crack and of the bending

moment which is applied to the rotor in the cracked section. These forces have $1x$ rev., $2x$ rev. and $3x$ rev. components. However, since the $1x$ rev. component due to the crack is generally masked by other effects (unbalance, bow), and the $3x$ rev. is generally very small, only the $2x$ rev. component is normally used in the identification procedure. In the case of a transverse crack, the approach according to equation (9) is convenient, where only $\mathrm{d}\mathbf{K}$ is different from zero. Due to the "breathing" mechanism of the crack during the rotation, the stiffness matrix is periodic and its Fourier expansion can be truncated at the third harmonic component.

$$\mathbf{K}(\Omega t) = \mathbf{K}_m + \Delta\mathbf{K}_1 \mathrm{e}^{\mathrm{i}\Omega t} + \Delta\mathbf{K}_2 \mathrm{e}^{\mathrm{i}2\Omega t} + \Delta\mathbf{K}_3 \mathrm{e}^{\mathrm{i}3\Omega t}. \tag{17}$$

The average term $\mathbf{K}_m$ then appears on the left side of equation (11), while the other terms generate $1x$ rev., $2x$ rev. and $3x$ rev. forces on the right side of equation (11), which can be rewritten in the following form, using an harmonic balance approach:

$$[-(n\Omega^2)\mathbf{M} + \mathrm{i}n\Omega\mathbf{D} + \mathbf{K}_m]\mathbf{X}_n \mathrm{e}^{\mathrm{i}n\Omega t} = -\Delta\mathbf{K}\mathrm{e}^{\mathrm{i}n\Omega t}(\mathbf{X}_{st} + \mathbf{X}_n \mathrm{e}^{\mathrm{i}n\Omega t}), \quad n = 1, 2, 3. \tag{18}$$

The equivalent force system (on the right side of equation (18)) is applied to the two nodes of the element which contains the crack and is therefore composed of a vector of eight generalized forces (in case of four-d.o.f. per node model). If equation (18) is used for the identification of an unknown crack, also $\mathbf{K}_m$ is unknown and is substituted by $\mathbf{K}$ of the uncracked shaft, from which it differs only very little. Among these forces it results from energy considerations that the most important ones are the bending moments which are rotating and roughly equal and opposite on the two nodes. Therefore, the unknowns are reduced to one bending moment M_n only for each harmonic component. The localization vector $[\mathbf{F}_L^{(k)}]$ and $\mathbf{A}^{(k)}$ have the following expressions:

$$\begin{aligned} &[\mathbf{F}_L^{(k)}] = [0 \vdots 0 \ i \quad 0 \ 1 \ 0 \quad -i \ 0 \quad -1 \vdots 0]^{\mathrm{T}}, \\ &\mathbf{A}^{(k)}(n) = M_n^{(k)} \mathrm{e}^{\mathrm{i}n\varphi^{(k)}}, \quad n = 1, 2, 3. \end{aligned} \tag{19}$$

Therefore, the crack is considered as a $2x$ rev. local bow in the identification procedure. It can further be shown that an axial asymmetry can be represented again by a set of $2x$ rev. external moments: this fault is then considered as a $2x$ rev. extended bow and the localization vector $[\mathbf{F}_L^{(k)}]$ has the same expression of equation (15) and $\mathbf{A}^{(k)}$ the same of equation (19).

2.4. JOURNAL OVALIZATION FAULT MODEL

When the rotating journal in an oil film bearing shows ovalization errors, then the rotor is forced through the oil film by a $2x$ rev. force, which depends on oil film stiffness and damping coefficients and on the ovalization error. Therefore, the model of the journal ovalization error is composed of two $2x$ rev. external forces in each bearing, whose amplitude generally decreases with the speed.

3. LEAST-SQUARES IDENTIFICATION METHOD

Now equation (11) can be rewritten, for each harmonic component, in the following way:

$$[\mathbf{E}(n\Omega)]\mathbf{X}_n = \sum_{i=1}^{m} \mathbf{F}_{f_n}^{(i)}(\Omega) = \mathbf{F}_{f_n}(\Omega), \tag{20}$$

where $[\mathbf{E}(n\Omega)]$ is the system dynamical stiffness matrix for the speed Ω and for the nth harmonic component. Nowadays, experimental vibration data of real machines are often collected by CM systems and are available for many rotating speeds, typically those of the run-down transient that, in large turbogenerators of power plants, occurs with slowly changing speed, due to the high inertia of the system, so that actually the transient can be considered as a series of different steady state conditions. This allows one to use these data in the frequency domain. The identification method can be applied for a set of p rotating speeds that can be organized as a vector:

$$\mathbf{\Omega} = [\Omega_1 \;\; \Omega_2 \;\; \cdots \;\; \Omega_p]^{\mathrm{T}}. \tag{21}$$

Then, matrix and vectors of equation (20) have to be expanded:

$$[E(n\mathbf{\Omega})]\mathbf{X}_n = \begin{bmatrix} \mathbf{E}(n\Omega_1) & 0 & 0 & 0 \\ 0 & \mathbf{E}(n\Omega_2) & 0 & 0 \\ \vdots & \vdots & \vdots & \vdots \\ 0 & 0 & 0 & \mathbf{E}(n\Omega_p) \end{bmatrix} \begin{bmatrix} \mathbf{X}_n \\ \mathbf{X}_n \\ \vdots \\ \mathbf{X}_n \end{bmatrix} = \begin{bmatrix} \sum_{i=1}^{m} \mathbf{F}_{f_n}^{(k)}(\Omega_1) \\ \sum_{i=1}^{m} \mathbf{F}_{f_n}^{(k)}(\Omega_2) \\ \vdots \\ \sum_{i=1}^{m} \mathbf{F}_{f_n}^{(k)}(\Omega_p) \end{bmatrix} = \mathbf{F}_{f_n}(\mathbf{\Omega}). \tag{22}$$

Under a formal point of view, it is unimportant to consider one or p rotating speeds in the identification. The fault vector is the sum of all the faults that affect the rotor as stated in equation (12). Matrix $[\mathbf{E}(n\mathbf{\Omega})]$ can be inverted and equation (20) becomes

$$\mathbf{X}_n = [\mathbf{E}(n\mathbf{\Omega})]^{-1} \cdot \mathbf{F}_{f_n}(\mathbf{\Omega}) = \alpha_n(\mathbf{\Omega}) \cdot \mathbf{F}_{f_n}(\mathbf{\Omega}), \tag{23}$$

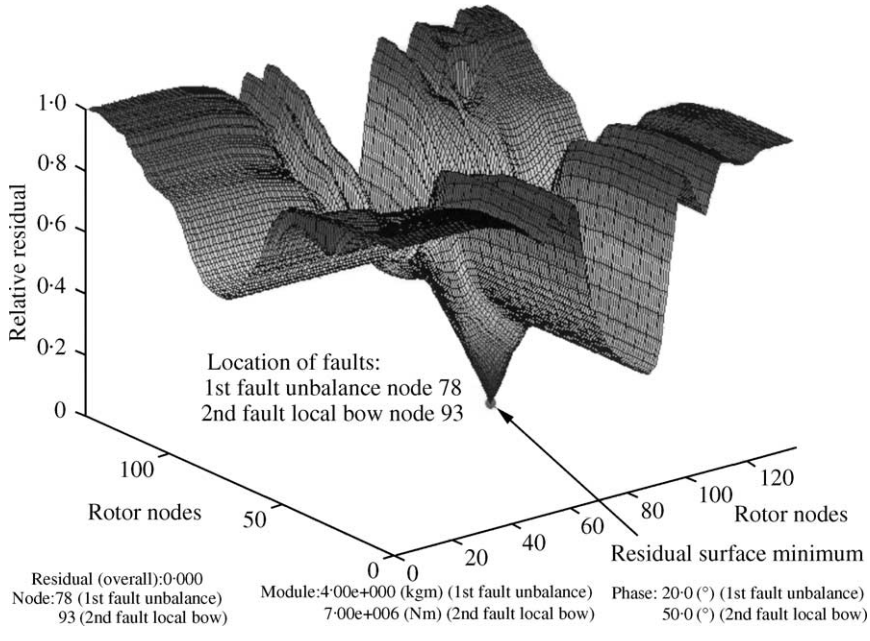

Figure 3. Residual surface in case of simultaneous identification of two faults. The location of the faults is in the minimum of the surface.

where $\alpha_n(\mathbf{\Omega})$ is the inverse of $[\mathbf{E}(n\mathbf{\Omega})]$. Reordering in a suitable way the lines in equation (23), by partitioning the inverse of the system dynamical stiffness matrix, and omitting from α_n and $\mathbf{F}_{f_n}$ the possible dependence on $\mathbf{\Omega}$ for conciseness, we obtain

$$\mathbf{X}_{B_n} = \alpha_{B_n} \cdot \mathbf{F}_{f_n}, \quad \mathbf{X}_{A_n} = \alpha_{A_n} \cdot \mathbf{F}_{f_n}, \tag{24}$$

where $\mathbf{X}_{B_n}$ is the complex amplitude vector representing the measured absolute vibrations in correspondence with the measuring sections and $\mathbf{X}_{A_n}$ is the vector of the remaining d.o.f. of the rotor system model.

Using the first set of equations (24), the differences $\boldsymbol{\delta}_n$, between calculated vibrations $\mathbf{X}_{B_n}$ and measured vibrations $\mathbf{X}_{Bm_n}$ can be defined, for each harmonic component, as

$$\boldsymbol{\delta}_n = \mathbf{X}_{B_n} - \mathbf{X}_{Bm_n} = \alpha_{B_n} \cdot \mathbf{F}_{f_n} - \mathbf{X}_{Bm_n}. \tag{25}$$

The number of equations n_E (number of measured d.o.f.) is lower than the number n_F (number of d.o.f. of the complete system model), which is also the number of elements of $\mathbf{F}_{f_n}$. But, as said before, $\mathbf{F}_{f_n}$ becomes a vector with many null-elements, even if the fault is not one only, so that the number of unknown elements of $\mathbf{F}_{f_n}$ is smaller than the number of equations. The system therefore has no single solution for all the equations and one has to use the least-squares approach in order to find the solution (identified fault) that minimize the differences which are calculated for all the different rotating speeds which are taken into consideration.

A scalar relative residual may be defined by the root of the ratio of the squared $\boldsymbol{\delta}_n$, divided by the sum of the squared measured vibration amplitudes $\mathbf{X}_{Bm_n}$:

$$\delta_{r_n} = \left(\frac{[\alpha_{B_n} \cdot \mathbf{F}_{f_n} - \mathbf{X}_{Bm_n}]^{*\mathrm{T}} [\alpha_{B_n} \cdot \mathbf{F}_{f_n} - \mathbf{X}_{Bm_n}]}{\mathbf{X}_{Bm_n}^{*\mathrm{T}} \mathbf{X}_{Bm_n}} \right)^{1/2}. \tag{26}$$

By means of the hypothesis of localization of the fault, the residual is calculated for each possible node of application of each defect. This fact implies that, if we indicate with z_k the abscissa along the rotor in correspondence to the kth fault among m faults, the relative residual in equation (26) is a surface in a $\mathbb{R}^{m+1}$ space, in other terms:

$$\delta_{r_n} = f(z_1, z_2, \ldots, z_k, \ldots, z_m). \tag{27}$$

Where the residual reaches its minimum, i.e., the minimum of the surface in equation (27), there is the most probable position of the fault. Figure 3 shows an example of the residual surface. The corresponding values of $\mathbf{F}_{f_n}$ give the modulus and the phase of the identified faults. The relative residual gives also an estimate of the quality of the identification, since it results the closer to zero the better the identified fault corresponds to the actual one; this follows easily from the analysis of equation (26).

Even if theoretically possible, some considerations are related to the actual interest of identifying more than two faults. First of all, in actual machines the occurrence of more than two simultaneous faults is very unusual. Second, the calculation time needed for the identification can become very large for more than two faults. This can make an on-line identification impossible. In a first approximation calculation time grows linearly with the number n_{speeds} of the rotating speed $\mathbf{\Omega}$ used in the identification procedure. If the model has $n_{elements}$, and T is the cycle time on the used computer, the times needed are approximately

$$n_{speeds} n_{elements} T \quad \text{for the identification of a fault,} \tag{28}$$

$$n_{speeds} \frac{n_{elsements}(n_{elements} + 1)}{2} T \quad \text{for the identification of two faults of the same type,} \tag{29}$$

$$n_{speeds} n_{elements}^2 T \quad \text{for the identification of faults of different types.} \tag{30}$$

Another important note is that the plotting of the relative residual is possible in the case of one or two faults only.

4. NUMERICAL SIMULATIONS

The proposed method has been tested on different types of machines, with different types of simultaneous faults. Due to the limited space available for the paper, in the following, only some numerical cases of one and two faults are presented on a machine type.

The machine model is a 320 MW turbogenerator composed of a HP-IP turbine, an LP turbine and a generator. The overall length of the machine is about 28 m, the mass is about 127 000 kg and seven oil-film bearings support the unit. The model of the rotor is composed of 74 elements (Figure 4), the first critical speed of HP-IP turbine is about 2000 r.p.m. and that of LP turbine is about 1800 r.p.m. The bearing stiffness and damping coefficients are available for rotating speeds in the range 300–3000 r.p.m. (an example is shown in Figure 5 for bearing $\#1$). The foundation is modelled by seven two-d.o.f. pedestal (mass, spring and damper systems) with constant mass, stiffness and damping coefficients.

Eight different cases of one and two faults have been analyzed on this model, which are summarized in Table 1. The single-fault cases includes two unbalances and a crack, the latter with three harmonic components. As regards two faults, the criterion used is to test the capability of the method to find not only the faults but also to discriminate among them even in the case they are applied to the same rotor of the machine, in positions which are close to each other. So the faults chosen are unbalances (that are very common in real machines and are function of the rotating speed) and moments that model several types of faults. The data used for the identification have been generated by means of simulation.

In order to evaluate the robustness of the proposed method to modelling errors, the identification procedure has been performed not only by means of the same models of rotor, bearing and pedestals used to generate the data, but also by means of a mistuned model of the system, in which some errors have been introduced in the bearing stiffness and damping coefficients. The choice of introducing some noise in the bearing coefficient has been done since these are usually most affected by errors, whether they are calculated or experimentally determined. A random noise of maximum amplitude 20% of the value has been applied to each bearing coefficient at each rotating speed (see Figure 5).

As regards one fault, the relative residual surface becomes a curve that can be displayed along with a model of the rotor, where the fault location is highlighted. The method identifies exactly the position, the module and the phase of the fault, when the bearings has no noise. The results are reported in Figures 6, 8, 10, 12 and 14, while the results in case of 20% noise are shown in Figures 7, 9, 11, 13 and 15. In these last cases, the results are also summarized in Table 2.

The results in Table 2 show that the identification method gives very good results also in the case of bearings with noise, the relative residual is small and the position, the module and the phase of the fault are identified with good accuracy.

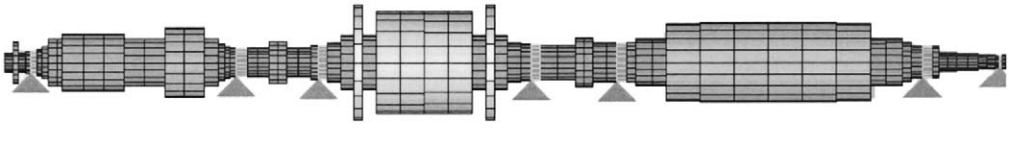

Figure 4. Rotor model of a 320 MW turbogenerator.

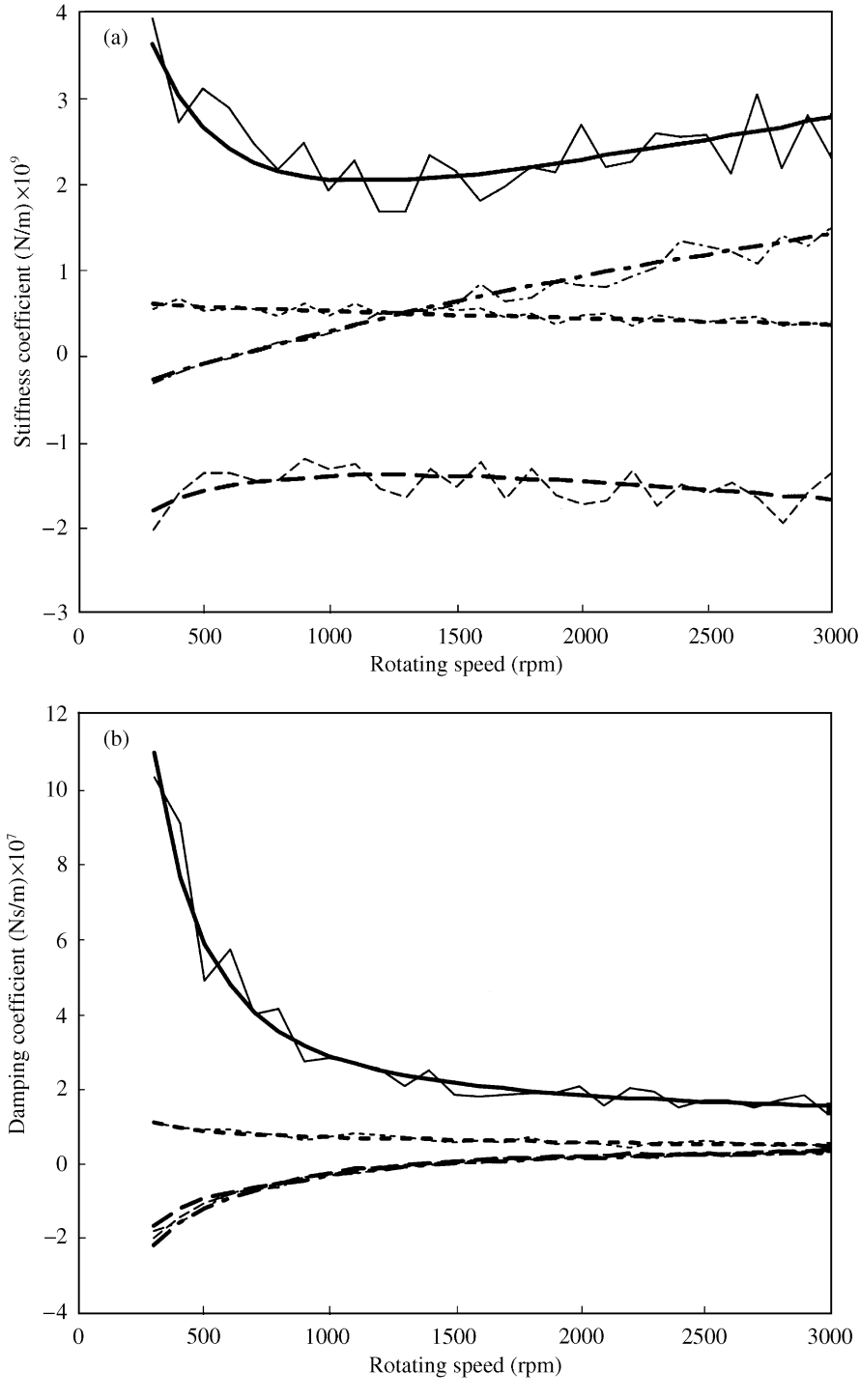

Figure 5. Bearing #1 stiffness and damping coefficients of 320 MW turbogenerator; —— represent the coefficients corrupted by noise. —— k_{xx}; – – – k_{xy}; – – – k_{yx}; – – – k_{yy}; —— r_{xx}; – – – r_{xy}; – – – r_{yx}; – – – – r_{yy}.

TABLE 1

Fault types used to generate the simulated data used in fault identification procedure

Case	Fault type	Node	Module	Phase
		One fault		
Case 1	Unbalance	12	1 kg m	40°
Case 2	Unbalance	32	1 kg m	10°
Case 3	Moments (1x)	33	7e6 N m	35′
	Moments (2x)	33	4e6 N m	35°
	Moments (3x)	33	2e6 N m	35°
		Two faults		
Case 4	Unbalance	12	1 kg m	10°
	Unbalance	32	5 kg m	25°
Case 5	Unbalance	12	2 kg m	30°
	Unbalance	15	1 kg m	0°
Case 6	Moments	33	1e6 N m	10°
	Moments	38	2e6 N m	30°
Case 7	Moments	14	2e6 N m	10°
	Moments	40	3e6 N m	25°
Case 8	Unbalance	32	1 kg m	20°
	Unbalance	40	7e6 N m	50°

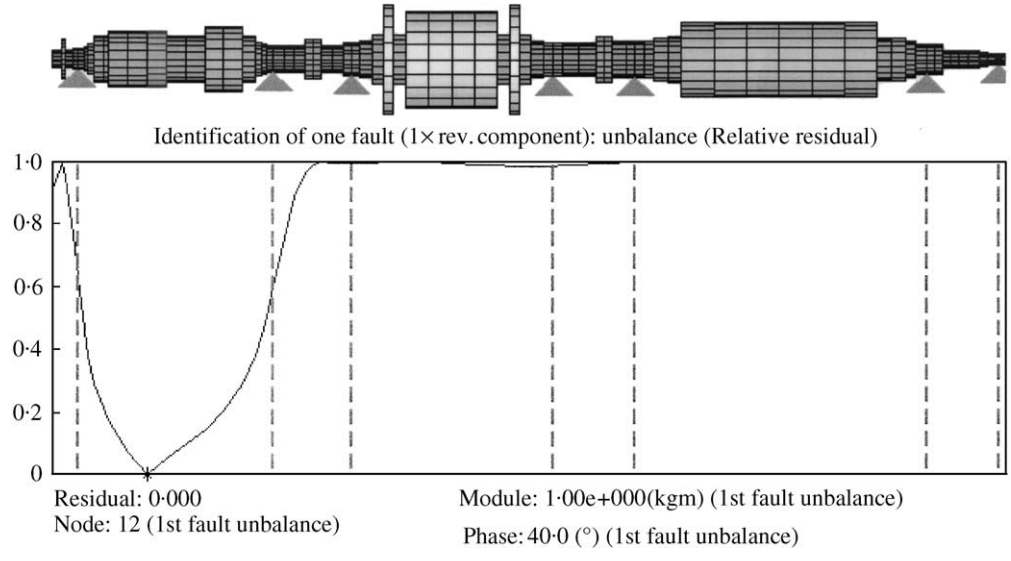

Figure 6. Identification results for case 1, bearings with no noise.

The results of two-fault identification procedure, without noise in the bearings, are reported in Figures 16, 18, 20, 22 and 24 by means of a representation called "*residual map*". This type of representation has been developed in order to give an effective and immediate representation of two-fault location along the rotor. The map is essentially a contour plot of the relative residual curve shown in Figure 3, where the colour coding, as shown on the right-hand side of each map, gives the quote, which corresponds to the effectiveness of the

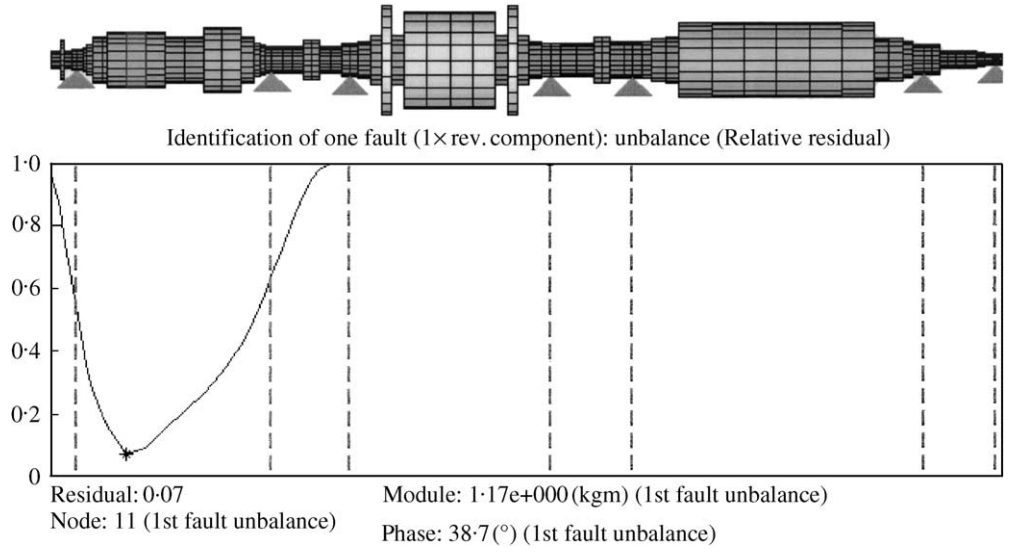

Figure 7. Identification results for case 1, bearings with 20% noise.

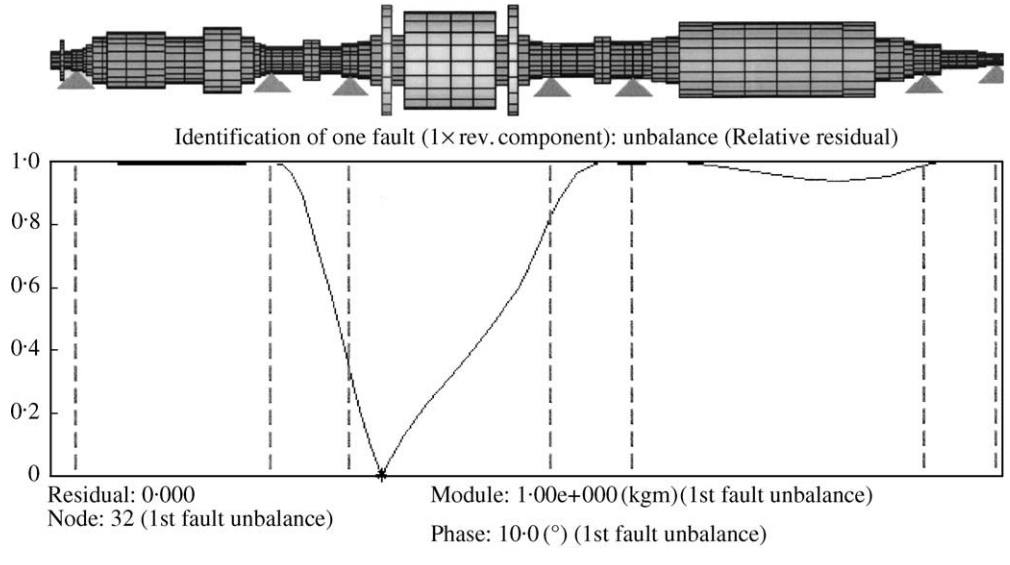

Figure 8. Identification results for case 2, bearings with no noise.

identification (a 0 residual indicates that the faults have been correctly identified in position, module and phase) and is the key for finding the position of the minimum. Along the η and ξ axes of the map, a rotor model is drawn and a label indicates the fault-type represented. The nodes where the faults are identified are highlighted.

Residual maps have different properties depending whether or not the faults are of same type. If two faults are of same type, as shown in Figures 16–22, the map is symmetric with respect to $\eta = \xi$. This is due to the fact that during the least-squares fitting, a double-loop cycle is executed on the rotor nodes, for instance z_1 and z_2, to position the fault forces $\mathbf{F}_{fn}^{(1)}$ and $\mathbf{F}_{fn}^{(2)}$, but due to the linearity of the system it is equal to apply them in this or in the reverse order. So the first cycle is executed for all the z_1 positions, while the second cycle can

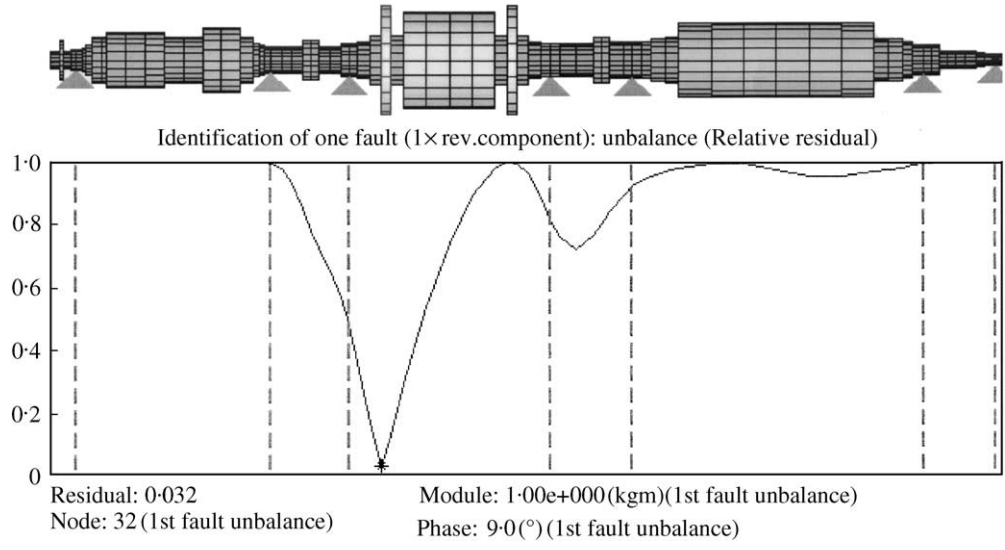

Figure 9. Identification results for case 2, bearings with 20% noise.

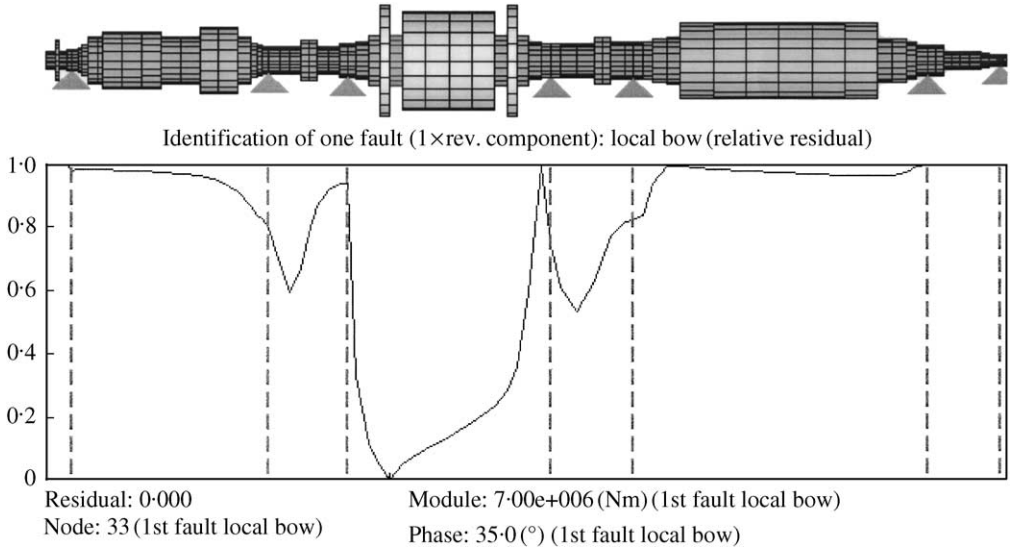

Figure 10. Identification results for case 3, 1*x*, bearings with no noise.

be executed only when $z_2 \geqslant z_1$. The triangular map obtained is then mirrored to obtain the complete map. This explains the calculation time saving in equation (29), when two faults are of same kind. Moreover, two positions are highlighted on both the rotor drafts to indicate the position of the faults of same kind and two minimums are present, in which the fault positions are permutated (see for instance Figure 16).

When two faults are of different kinds, the order of applying the forces is important, i.e., the effect of a moment $\mathbf{F}_{fn}^{(1)}$ in the node z_1 is different from the effect of a force $\mathbf{F}_{fn}^{(2)}$ in the same node. Therefore, the two loops have to be executed completely and this explains that in this case the calculation time is given by equation (30). The residual map in this case is not

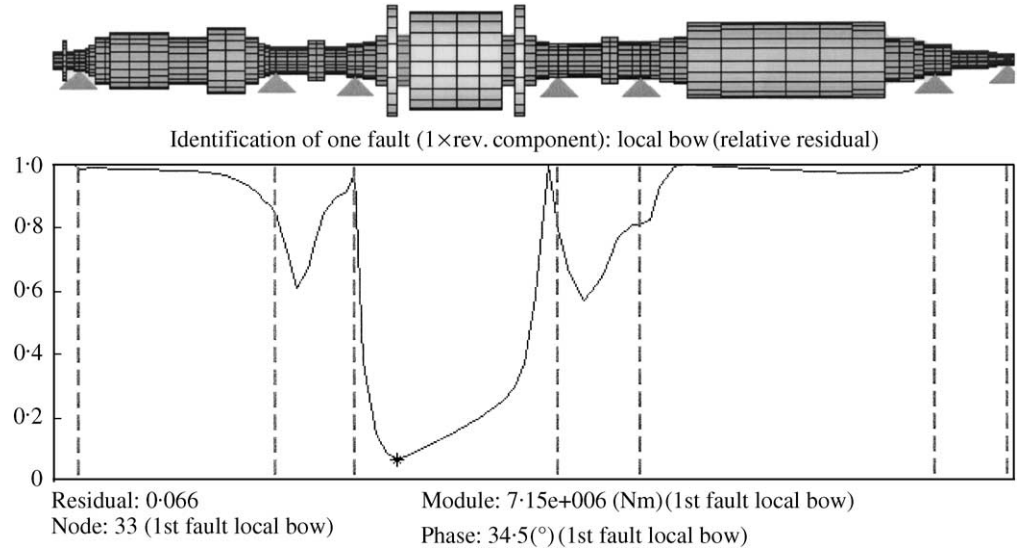

Figure 11. Identification results for case 3, 1*x*, bearings with 20% noise.

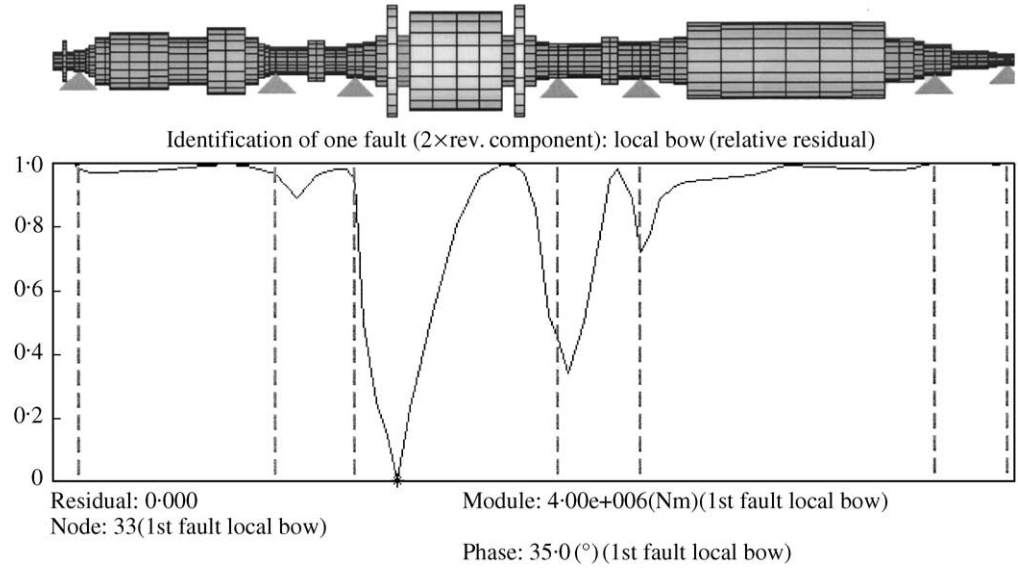

Figure 12. Identification results for case 3, 2*x*, bearings with no noise.

symmetric and has a minimum only. The positions highlighted on the rotors are different and each rotor indicates a different fault (see for instance Figure 24).

About the results of the identification, without noise in the bearings, the faults are exactly identified in all the proposed cases, since the relative residual is zero and the module and phases (not reported for conciseness) are those used to generate the data. The maps in Figures 16 and 18 are relative to the identification of two unbalances and the second shows that the method has identified two simultaneous unbalances on the same machines (the HP-IP turbine).

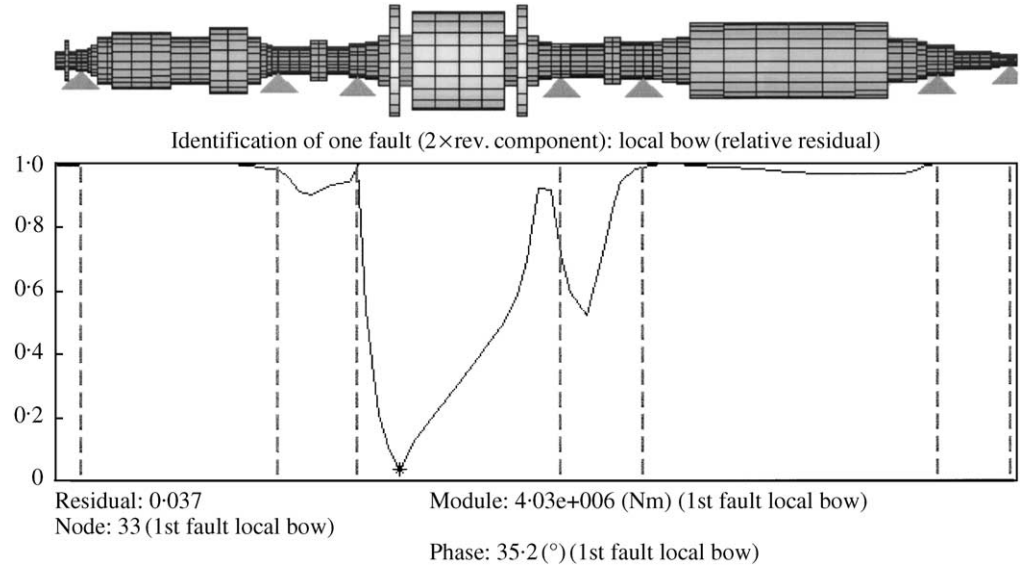

Figure 13. Identification results for case 3, 2*x*, bearings with 20% noise.

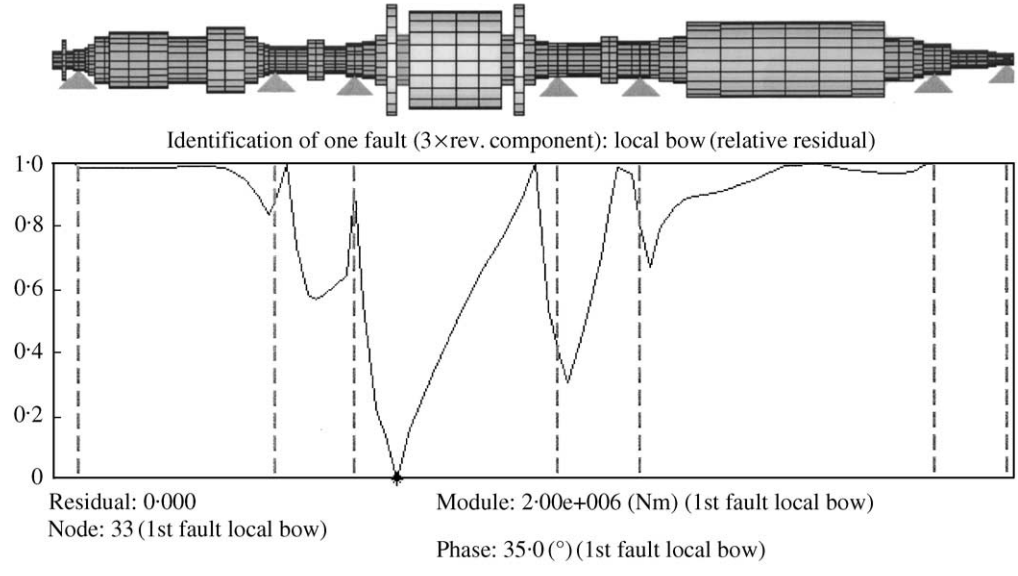

Figure 14. Identification results for case 3, 3*x*, bearings with no noise.

In Figures 20 and 22, the two local bows are exactly identified, also when they are applied on the same machine, the HP-IP turbine again. The last map, in Figure 24, shows the correct identification of two faults of a different kind on the same machine, the LP turbine in this case.

The results of two-fault identification with noise in the bearings are reported in the residual maps in Figures 17, 19, 21, 23 and 25 and summarized in Table 3.

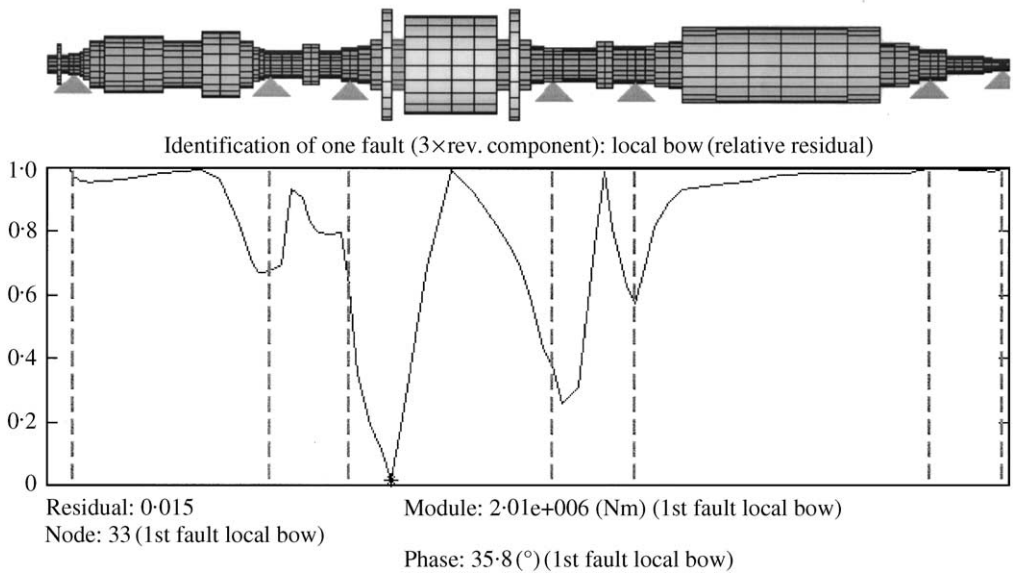

Figure 15. Identification results for case 3, 3*x*, bearings with 20% noise.

TABLE 2

Summary of identification procedure for one fault and bearing with noise

	One fault				20% noise in the bearings					
Case	Fault type	Node	Module	Phase	Residual	Node	Module	Phase	Error on module	Error on phase
Case 1	Unbalance	12	1 kg m	40°	0·070	11	1·17 kg m	38·7°	17%	− 0·7%
Case 2	Unbalance	32	1 kg m	10°	0·032	32	1 kg m	9°	0%	− 0·6%
	Mom. (1*x*)	33	7e6 N m	35°	0·066	33	7·15e6 N m	34·5°	2%	− 0·3%
Case 3	Mom. (2*x*)	33	4e6 N m	35°	0·037	33	4·03e6 N m	35·2°	1%	0·1%
	Mom. (3*x*)	33	2e6 N m	35°	0·015	33	2·01e6 N m	35·8°	1%	0·4%

The results in Table 3 show that the two-fault identification is less accurate than one fault identification when there are modelling errors, i.e., when the models of the bearings have random noise. Some considerations can be drawn: (1) the identification is more accurate when the faults are on different machines (cases 4 and 7); (2) the identification of the moments is more precise than that of the unbalances. The values in the wrong node in case 6 should be considered as they are, since the moments are applied, in this case, on an element that has different diameter and length with respect to the original element. In this case, instead of the absolute value of the moments, the relative rotation of the element due to the moments should be compared, as it has been done for the error calculation in Table 3; (3) the method can handle two faults of different kind on the same rotor (case 8), but the unbalance identification is less precise again.

Anyway, the identification procedure shows to be quite robust with respect to modelling errors, not only in the case of one fault, as also verified by means of experimental results by Bachschmid and Pennacchi [8], but also in the case of two faults.

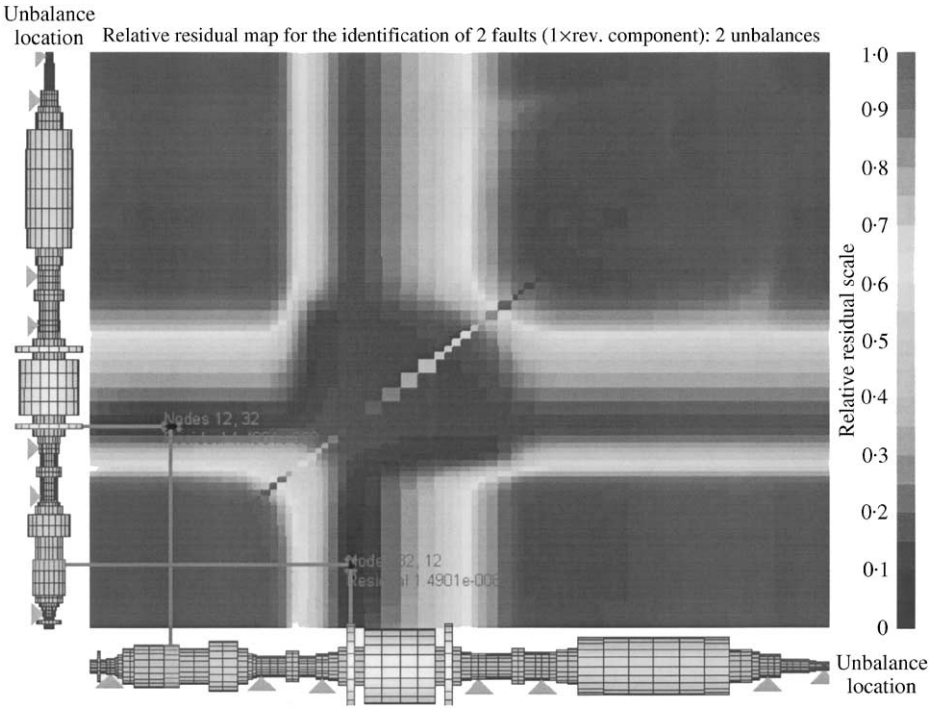

Figure 16. Residual map for case 4, bearings with no noise.

Figure 17. Residual map for case 4, bearings with 20% noise.

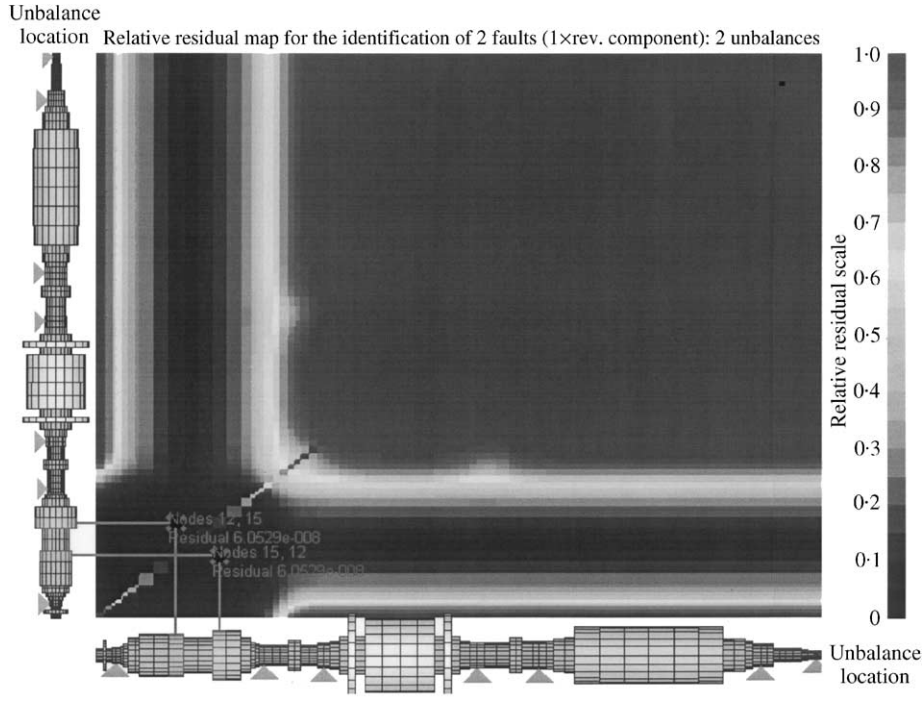

Figure 18. Residual map for case 5, bearings with no noise.

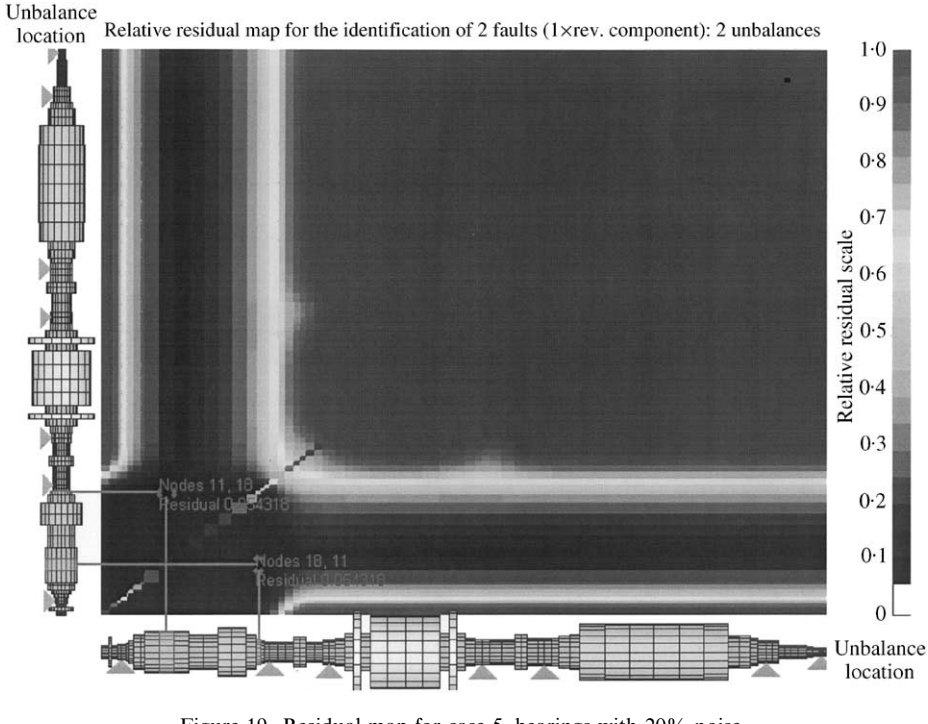

Figure 19. Residual map for case 5, bearings with 20% noise.

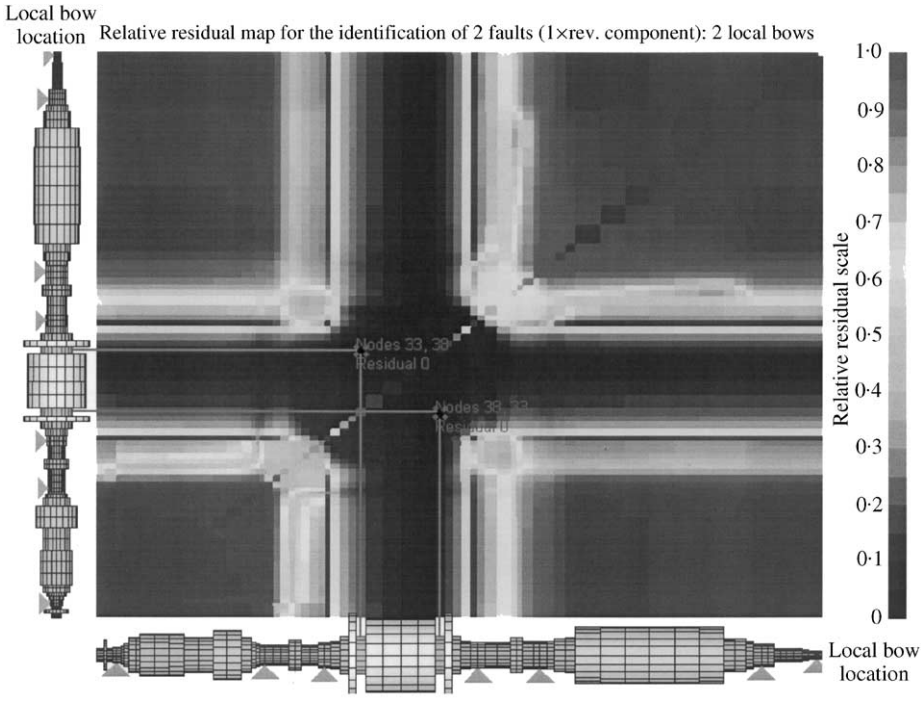

Figure 20. Residual map for case 6, bearings with no noise.

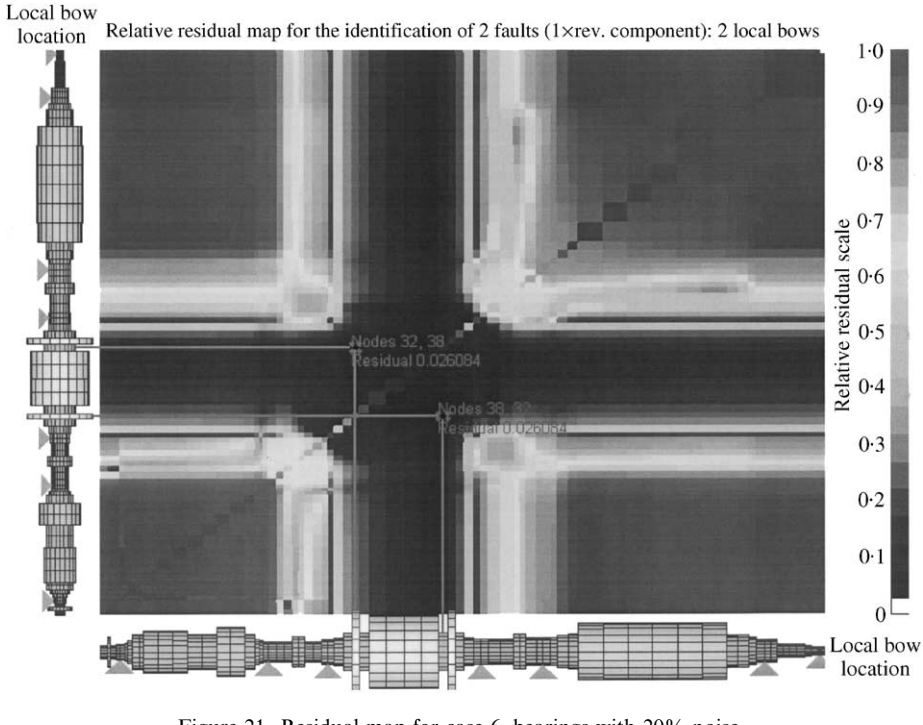

Figure 21. Residual map for case 6, bearings with 20% noise.

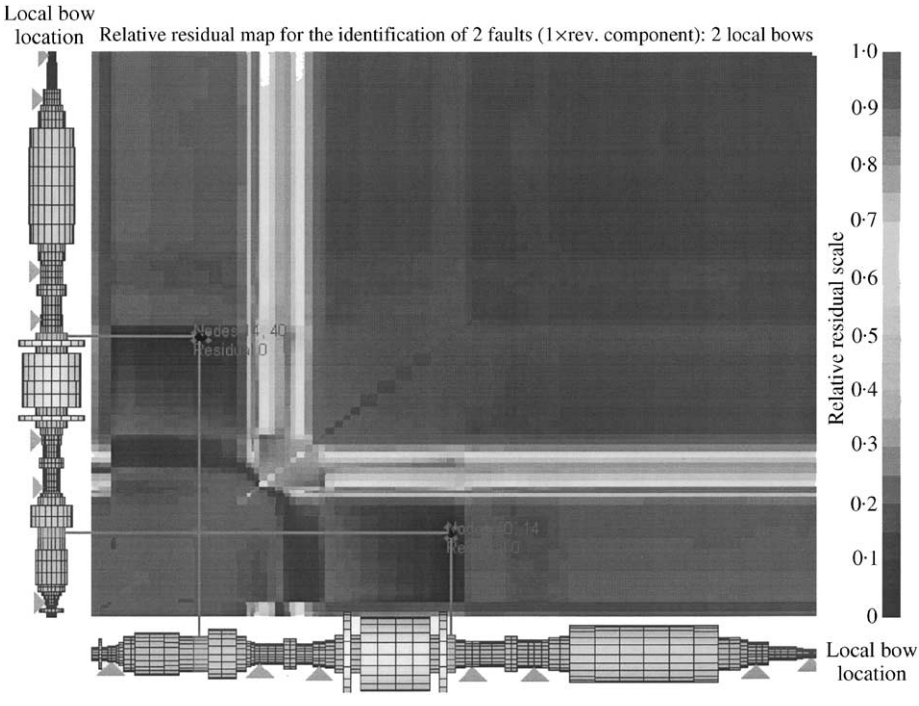

Figure 22. Residual map for case 7, bearings with no noise.

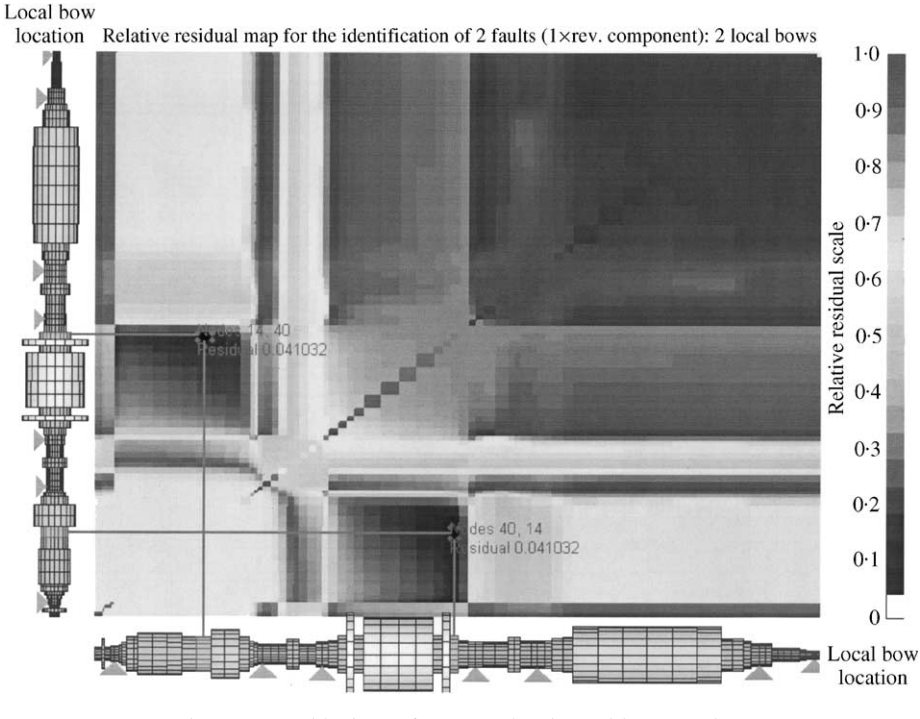

Figure 23. Residual map for case 7, bearings with 20% noise.

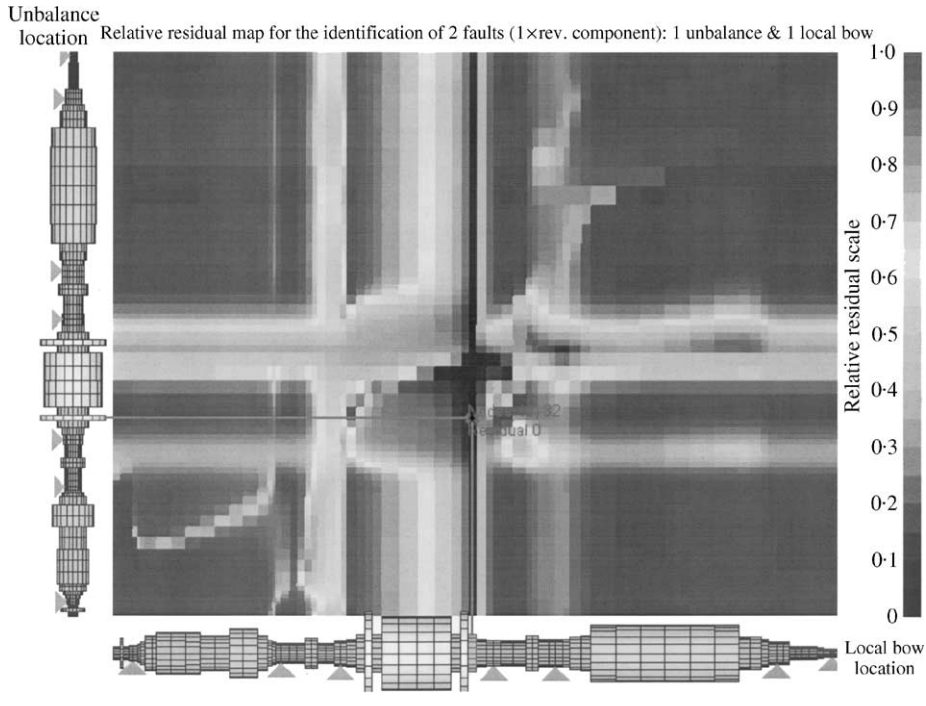

Figure 24. Residual map for case 8, bearings with no noise.

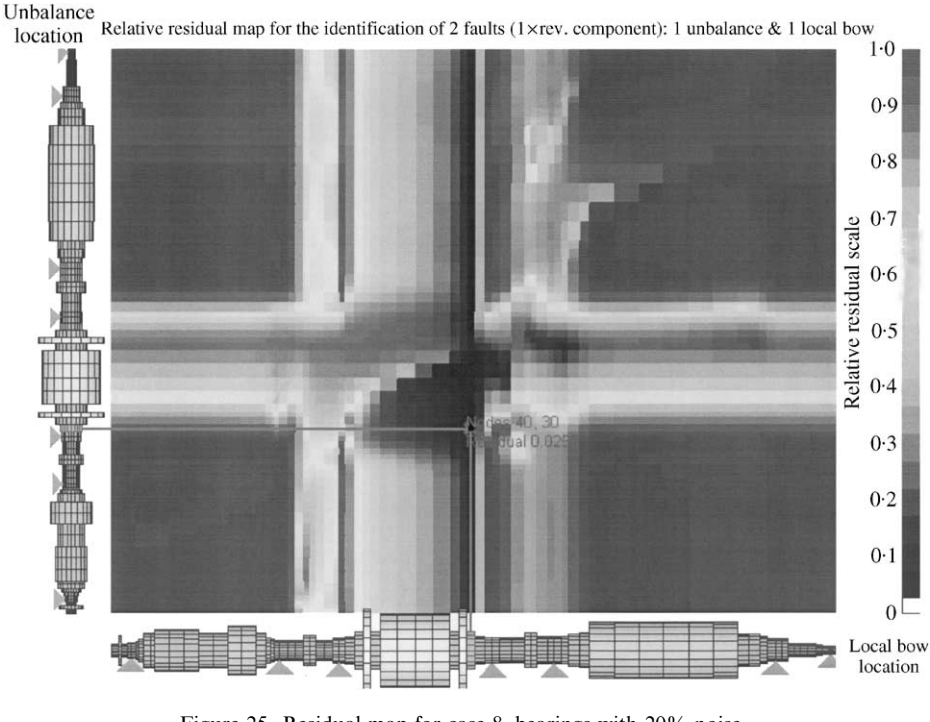

Figure 25. Residual map for case 8, bearings with 20% noise.

TABLE 3

Summary of identification procedure for two faults and bearings with noise

Two faults					20% noise in the bearings				Error on module	Error on phase
Case	Fault type	Node	Module	Phase	Residual	Node	Module	Phase		
Case 4	Unbalance	12	1 kg m	10°	0·069	12	0·983 kg m	9°	− 2%	− 0·6%
	Unbalance	32	5 kg m	25°		32	5·37 kg m	25·5°	7%	0·3%
Case 5	Unbalance	12	2 kg m	30°	0·054	11	3·31 kg m	22·7°	66%	− 4·1%
	Unbalance	15	1 kg m	0°		18	1·08 kg m	− 10·9°	8%	− 6·1%
Case 6	Moments	33	1e6 N m	10°	0·026	32	4·55e6 N m	− 7·3°	− 8%†	− 9·6%
	Moments	38	2e6 N m	30°		38	2·44e6 N m	33·7°	22%	2·1%
Case 7	Moments	14	2e6 N m	10°	0·041	14	2·01e6 N m	8·2°	1%	− 1·0%
	Moments	40	3e6 N m	25°		40	3·06e6 N m	26·6°	− 2%	0·9%
Case 8	Unbalance	32	1 kg m	20°	0·026	30	0·752 kg m	48·1°	− 25%	15·6%
	Moments	40	7e6 N m	50°		40	6·92e6 N m	48·1°	− 1%	− 1·1%

†The relative rotation on element 33 (length 0·397 m, outside stiffness diameter 0·750 m, inside stiffness diameter 0·195 m) with moments of 1e6 N m is 1·22e-4 rad, that of element 32 (length 0·254 m, outside stiffness diameter 1 m, inside stiffness diameter 0·195 m) with moments of 4·55e6 N m is 1·12e-4 rad.

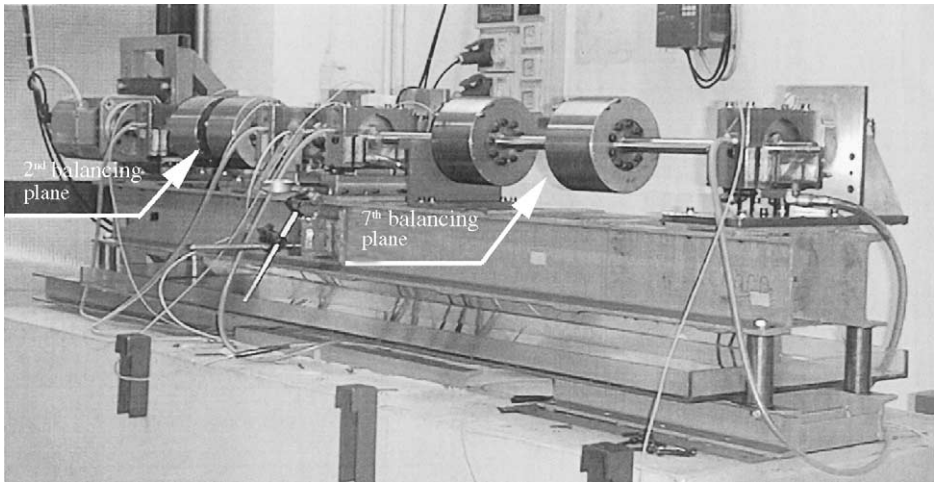

Figure 26. MODIAROT test-rig of Politecnico di Milano.

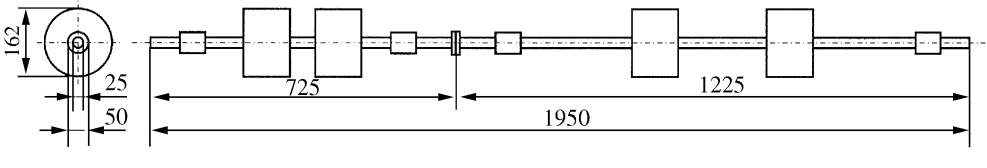

Figure 27. Sketch of MODIAROT test-rig shaft.

5. ANALYSIS OF EXPERIMENTAL DATA

The proposed method has been also tested by means of experimental results obtained on the MODIAROT (Brite Euram Contract BRPR-CT95-0022 MOdel based DIAgnostics in

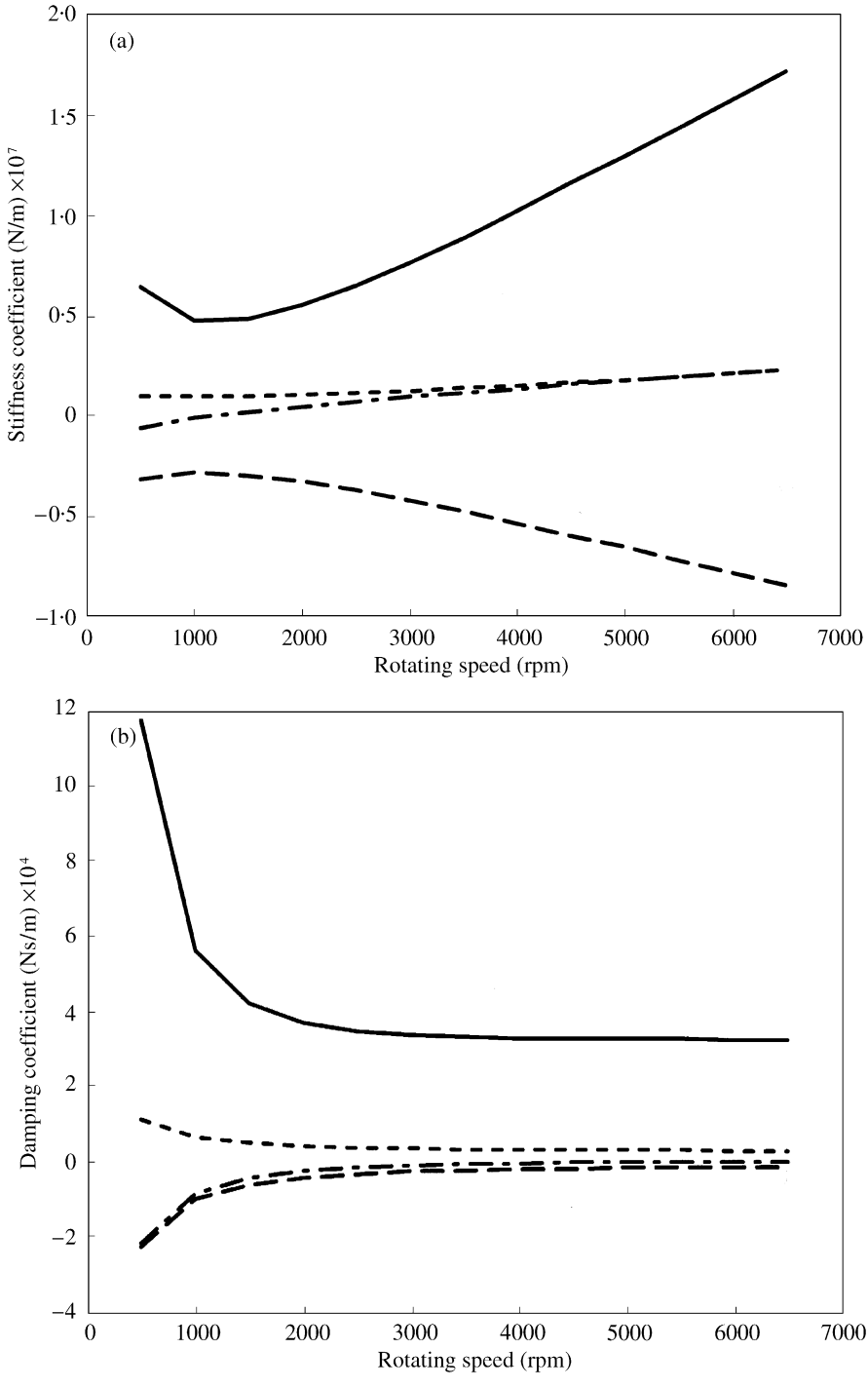

Figure 28. Bearing #3 stiffness and damping coefficients of MODIAROT test-rig. —— k_{xx}; – – – k_{xy}; – – – k_{yx}; – – – k_{yy}; —— r_{xx}; – – – r_{xy}; – – – r_{yx}; – – – – r_{yy}.

ROTating machines) test-rig designed by the Politecnico di Milano for analyzing the effects of different malfunctions on the dynamic behaviour of rotors. The test-rig, shown in Figures 26 and 27, is composed of two rigidly coupled rotors driven by a variable speed electric

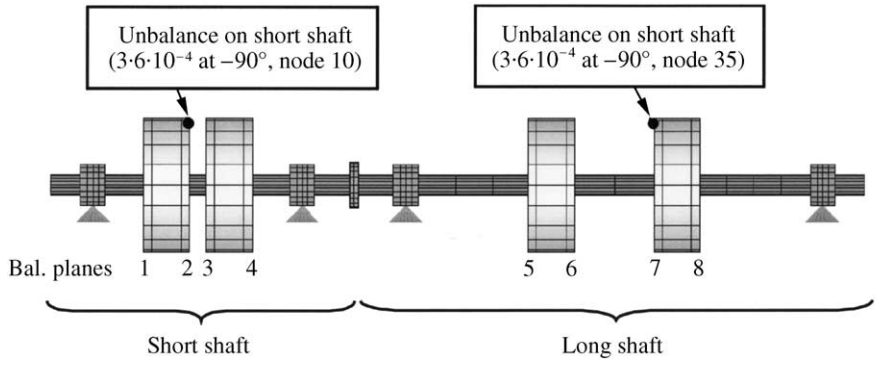

Figure 29. Unbalances on MODIAROT test-rig.

TABLE 4

Fault characteristics on MODIAROT test-rig of Politecnico di Milano

Type	Node	Module	Phase
Unbalance	10	3·6e-4 kg m	– 90°
Unbalance	35	3·6e-4 kg m	– 90°

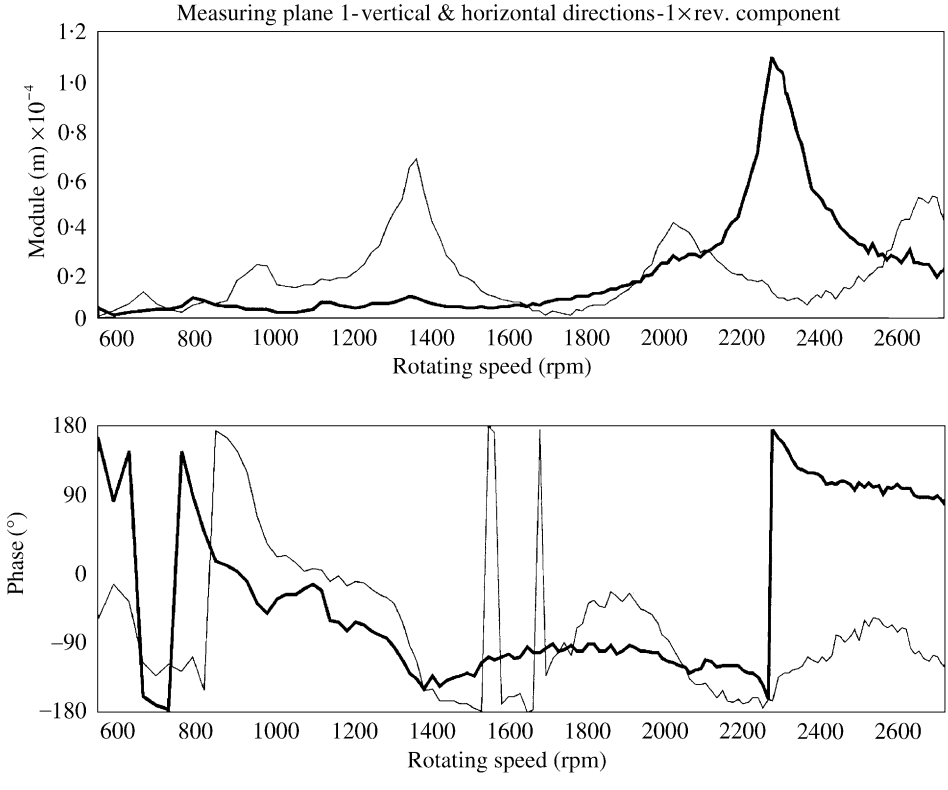

Figure 30. Experimental vibration differences in bearing #1. —Vertical; — Horizontal.

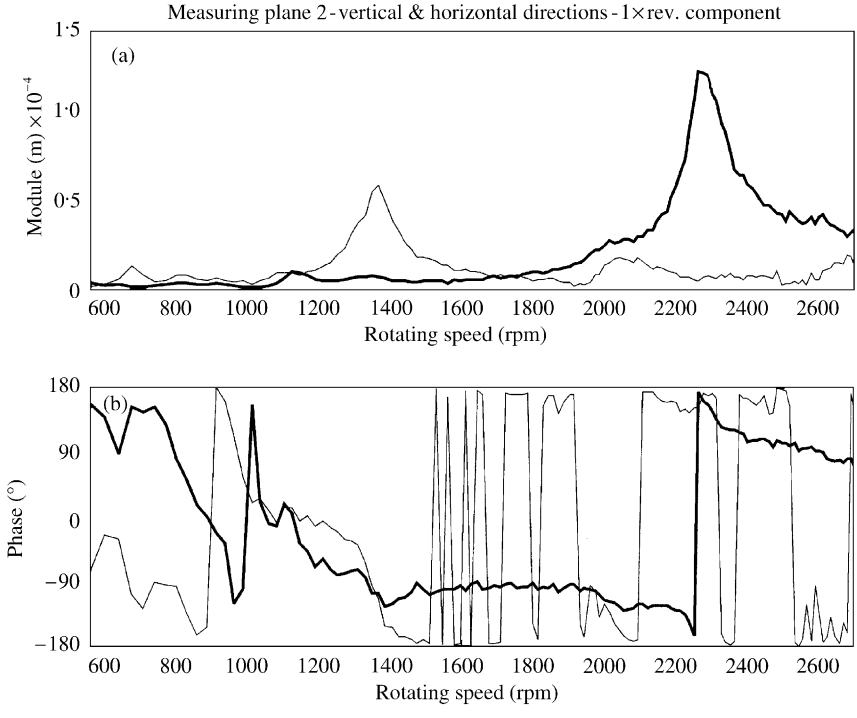

Figure 31. Experimental vibration differences in bearing #2. —— Vertical; — Horizontal.

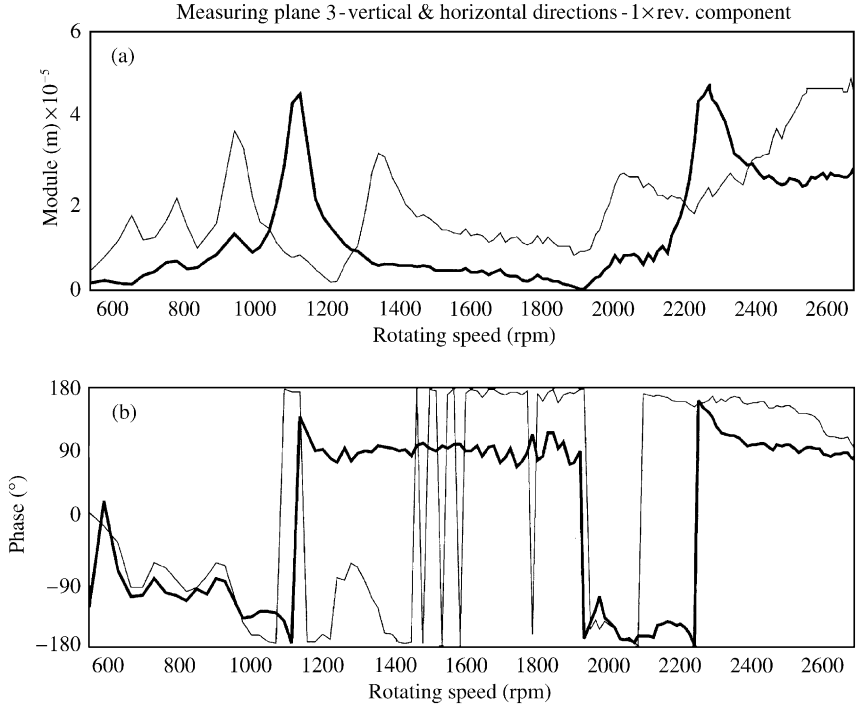

Figure 32. Experimental vibration differences in bearing #3. —— Vertical; — Horizontal.

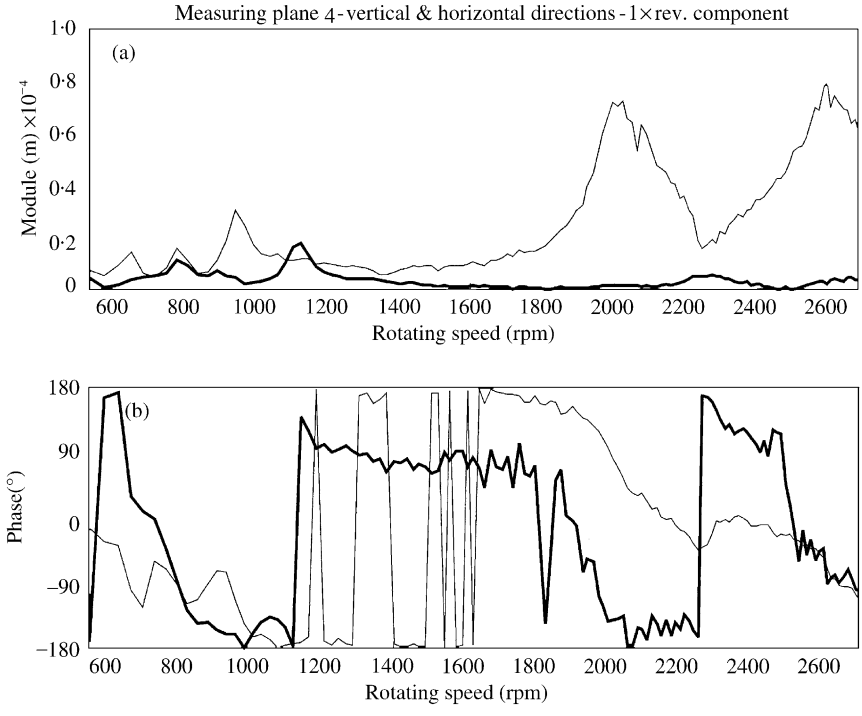

Figure 33. Experimental vibration differences in bearing #4. ——— Vertical; — Horizontal.

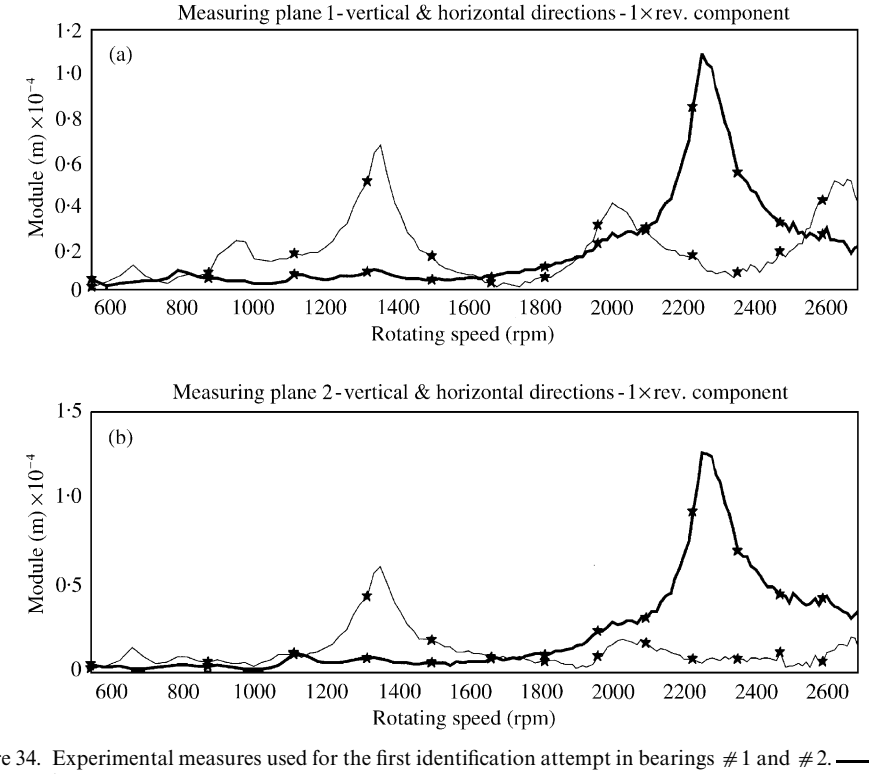

Figure 34. Experimental measures used for the first identification attempt in bearings #1 and #2. ——— Vertical; — Horizontal.

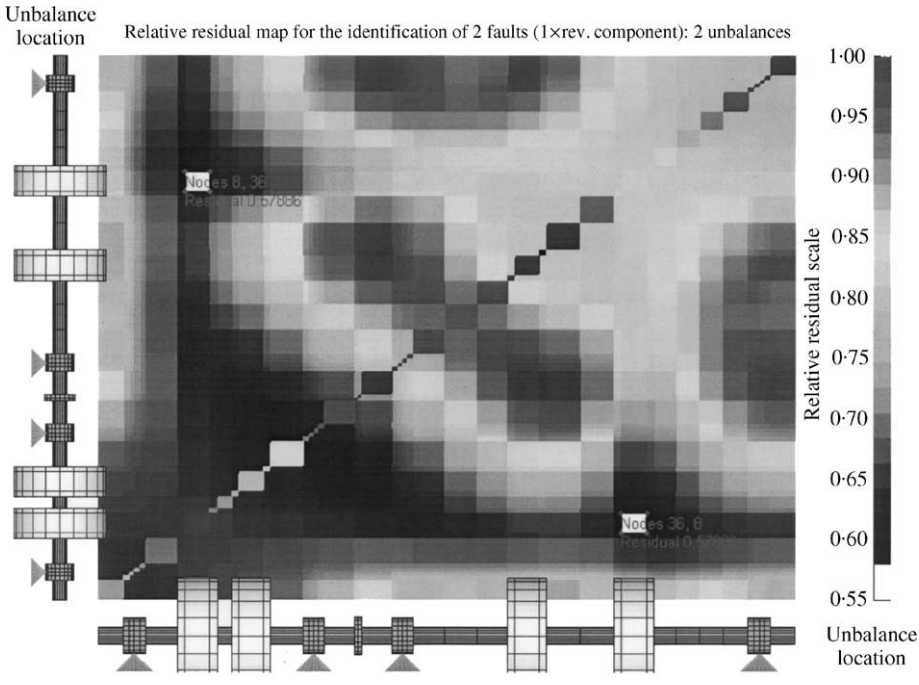

Figure 35. Residual map using the rotating speeds in the range 550–2700 r.p.m.

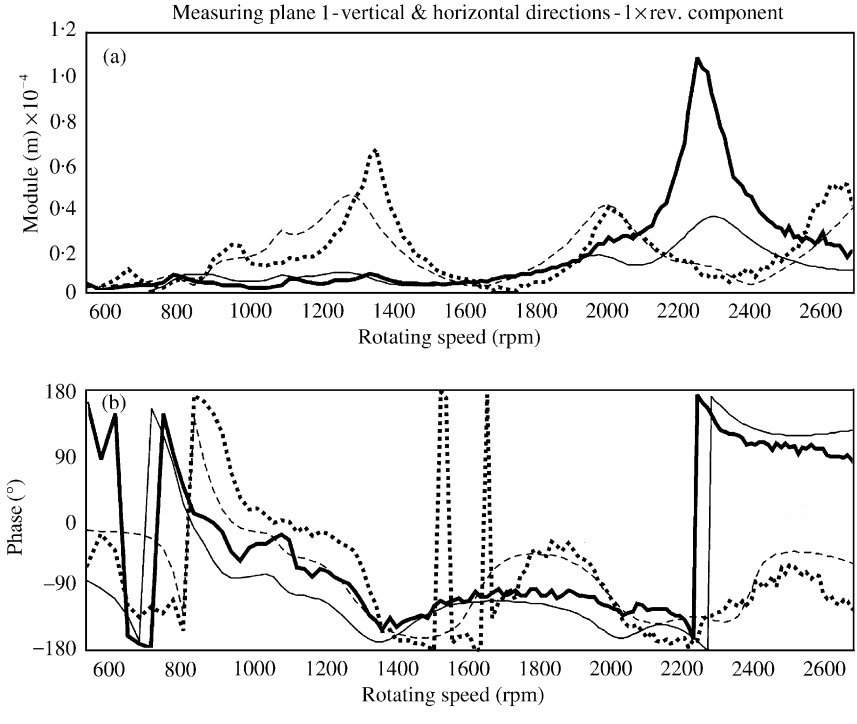

Figure 36. Comparison between experimental and analytical results using the rotating speeds in the range 550–2700 r.p.m. bearing #1. —— Experimental vertical; — Analytical vertical; ■■■■ Experimental horizontal; – – – Analytical horizontal.

TABLE 5

Identification results in the range 550–2700 *r.p.m.*

			550–2700 r.p.m						
Type	Node	Module	Phase	Residual	Node	Module	Phase	Error on module	Error on phase
Unbalance	10	3·6e-4 kg m	− 90°	0·579	8	4·2e-4 kg m	− 82·8°	17%	4%
Unbalance	35	3·6e-4 kg m	− 90°		36	3·81e-4 kg m	− 89·7°	6%	0·2%

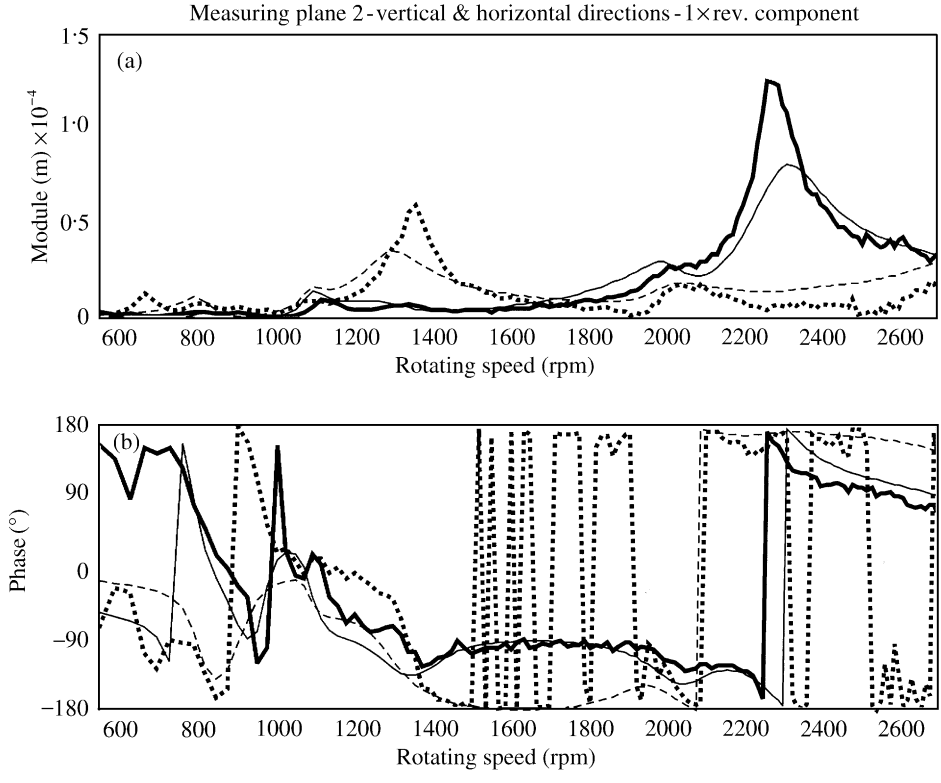

Figure 37. Comparison between experimental and analytical results using the rotating speeds in the range 550–2700 r.p.m. bearing #2. —— Experimental vertical; — Analytical vertical; ■■■■ Experimental horizontal; – – – Analytical horizontal.

motor and supported on four elliptical-shaped oil film bearings. An example of bearing stiffness and damping coefficients is reported in Figure 28. Both rotors are made of steel and the rotor train is long about 2 m and has a mass of about 90 kg. The rotors have three critical speeds within the operating speed range 0–6000 r.p.m., the model of the rotor has been tuned and the stiffness and damping coefficients of the bearings are determined with great accuracy as described in reference [10].

The rotor system is mounted on a flexible steel foundation, with several natural frequencies in the operating speed range. In this case, the foundation has been modelled by means of a modal representation and further details are reported in Vania *et al.* [14]. Two proximity probes in each bearing measure the relative shaft displacements, or the journal

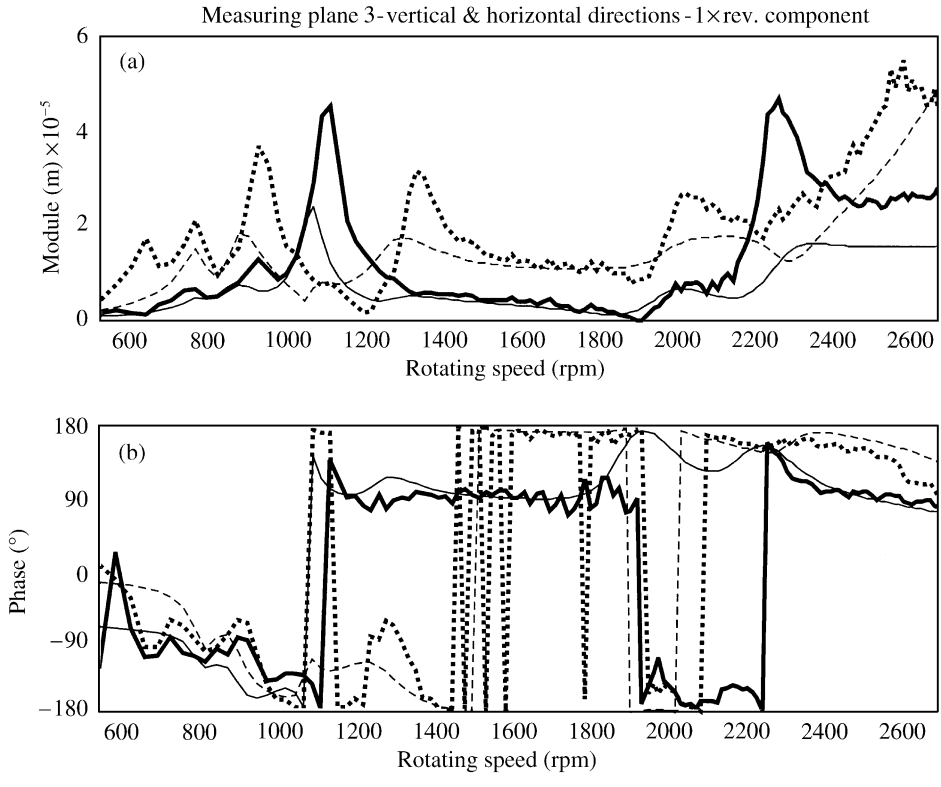

Figure 38. Comparison between experimental and analytical results using the rotating speeds in the range 550–2700 r.p.m. bearing #3. —— Experimental vertical; — Analytical vertical; ■■■■ Experimental horizontal; – – – Analytical horizontal.

orbits; two accelerometers on each bearing housing measure its vibrations, and two force sensors on each bearing housing measure the forces which are transmitted to the foundation. The absolute vibration of the shaft is calculated by adding the relative displacement measured by the proximitors to the absolute bearing housing displacement, which is obtained integrating twice the acceleration measured by the accelerometers. The force measurements were not used in this case.

A first run-down test was performed in order to obtain a reference vibration data (the vector $\mathbf{x}_1$ of equation (7)) due to the weight $\mathbf{W}$ and the unknown unbalance force $\mathbf{U}e^{i\Omega t}$ and unbalance moment $\mathbf{M}_u e^{i\Omega t}$. Then, in order to simulate two faults, two masses were added to the rotor on the second and seventh balancing plane (see Figure 29 and Table 4) and a second run-down was performed and the total vibration $\mathbf{x}_t$ was obtained. Then, the first measurements were subtracted from the last ones in order to obtain the vibration vector $\mathbf{x}$ due to the faults.

These difference vibration vectors are reported in Figures 30–33. The frequency response diagrams need some comments: (1) the first natural frequency of long shaft are about 950 r.p.m. in horizontal and 1150 r.p.m. in vertical direction; (2) the very high peak in vertical direction in Figures 30–32 corresponds to the third mode of the foundation (2256 r.p.m), while the others at 1350 and 2000 r.p.m. are horizontal modes of the foundation; (3) even if the test-rig is built to operate in the range 0–6000 r.p.m. the rotating speed at which the measurements are acquired is limited to the range 550–2700 r.p.m. the

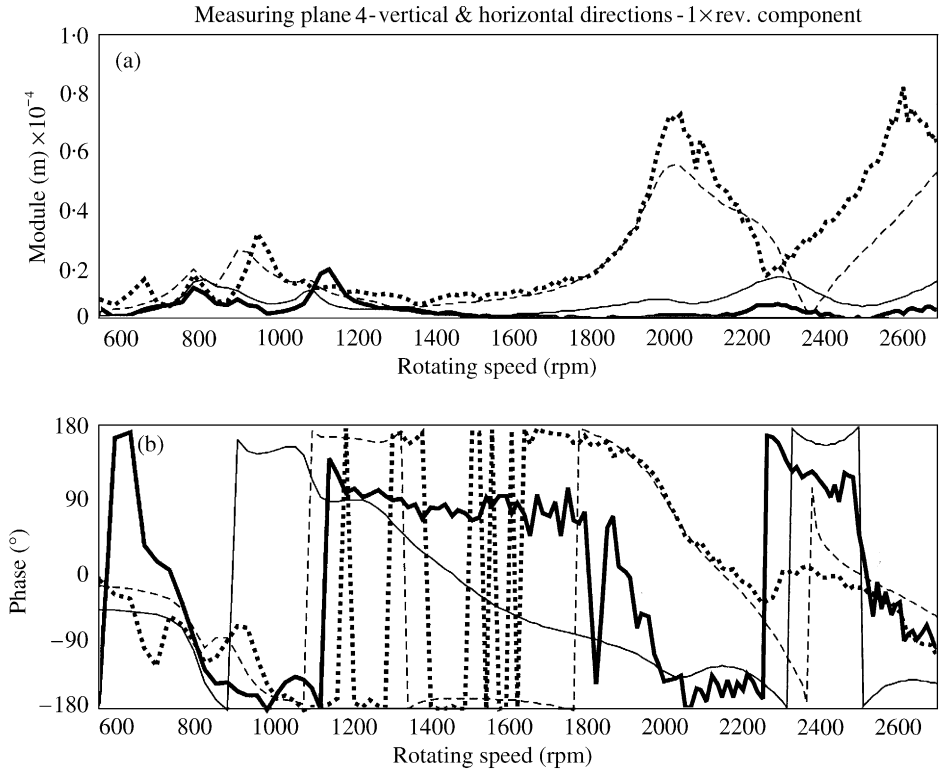

Figure 39. Comparison between experimental and analytical results using the rotating speeds in the range 550–2700 r.p.m. bearing #4. —— Experimental vertical; — Analytical vertical; ■■■■ Experimental horizontal; – – – Analytical horizontal.

upper limit is due to the fact that system non-linearities become more significant over 2700 r.p.m. and the model fitting is not so good as for lower rotating speeds.

The identification procedure can be performed as previously described in the numerical applications. Since in this case experimental data are used, some caution should be taken into account. Generally, the use of data close to the resonance peaks leads to a poor identification, also in the case of a fault only. Anyway, a first attempt has been done without taking into account this fact by choosing the measures corresponding to a set of 13 equally disturbed rotating speeds within the available range, as shown in Figure 34. The results of the identification are reported in the residual map in Figure 35 and in Table 5. Even if the relative residual of the identification in rather high, the location of the identified faults can be considered fairly good since they are on the same flywheel masses of the actual faults. The error on the phase is reduced, but this fact is quite common in least-squares identification, as so as that on the module. Similar results are obtained with different set of rotating speeds in the range 550–2700 r.p.m. The comparison between the theoretical response of the model to the identified faults and the experimental data is reported in Figures 36–39.

Even if the previous identification can be considered as quite good, it has been looked for improving the result. The first analysis that has been performed was the running of the identification of the two simultaneous faults by considering a rotating speed at once. This is shown in Figures 40 and 41, where the relative residual, the identified nodes, modules and phases are plotted as a function of the rotating speed. The best results, as expected, are

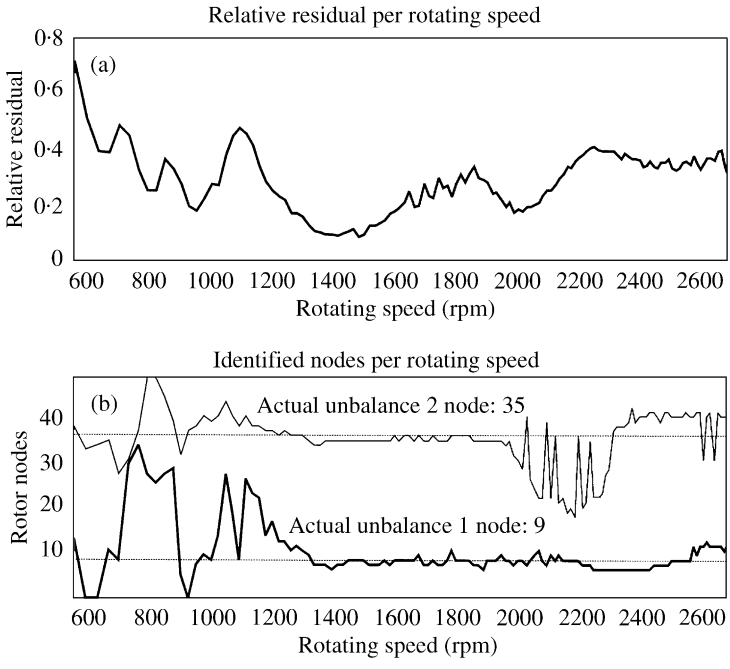

Figure 40. Relative residual and identified nodes using a rotating speed at once. — Unbalance 1; — Unbalance 2.

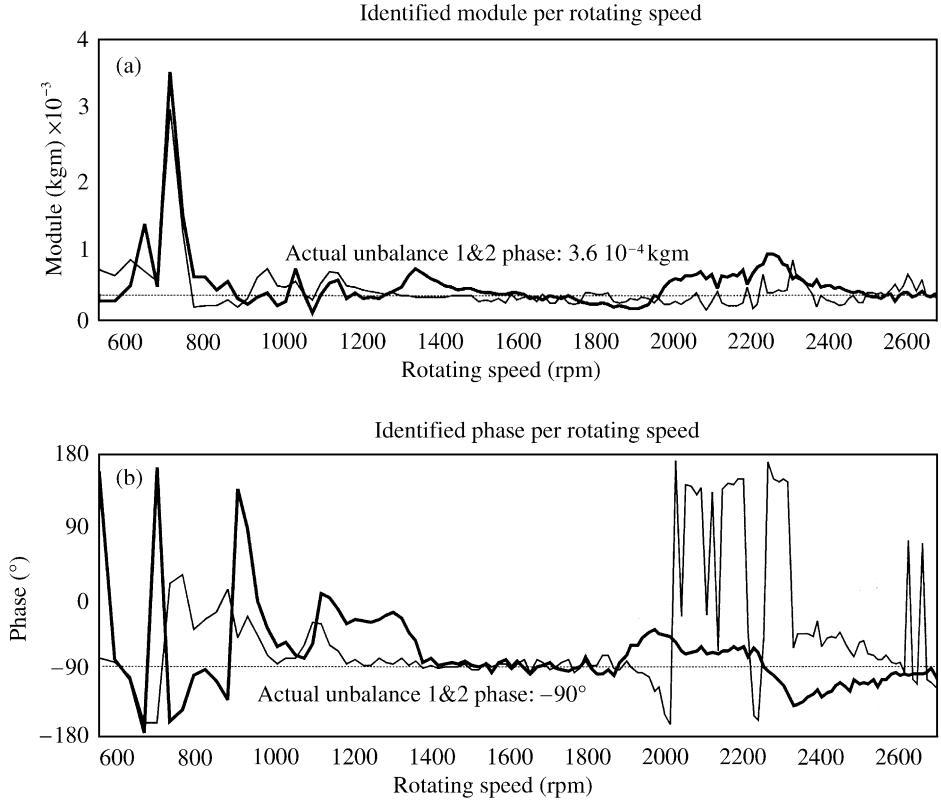

Figure 41. Identified modules and phase using a rotating speed at once. — Unbalance 1; — Unbalance 2.

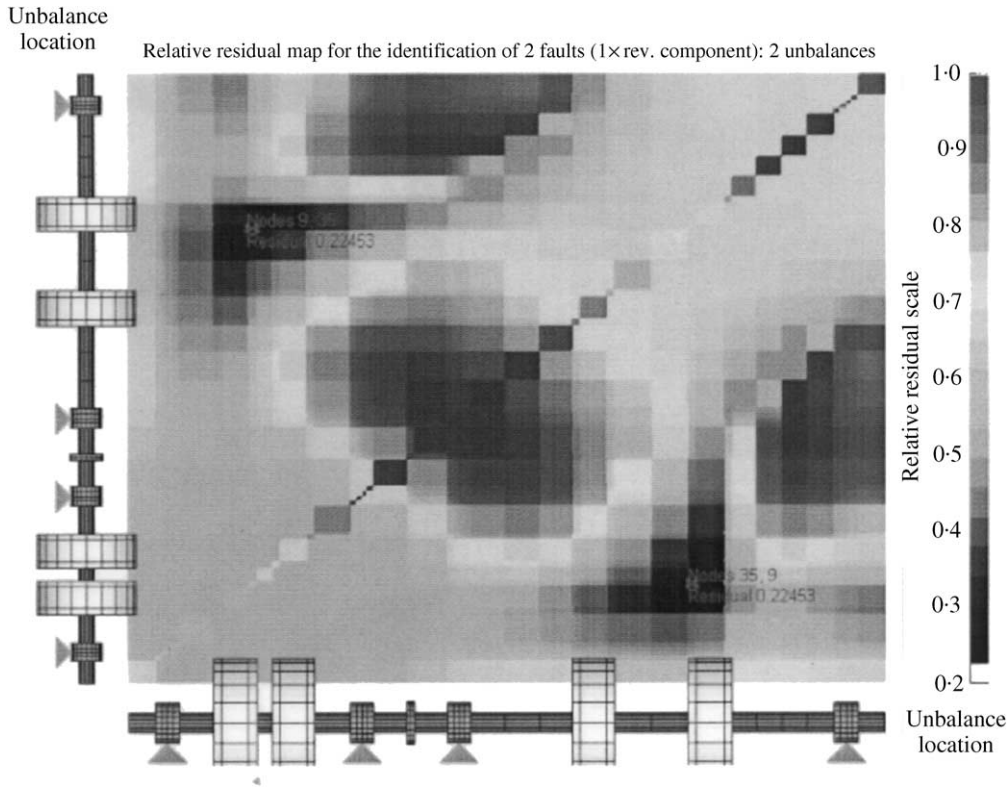

Figure 42. Residual map using a rotating speed of 1729 r.p.m.

TABLE 6

Identification results

Type	Node	Module	1729 r.p.m Phase	Residual	Node	Module	Phase	Error on module	Erron on phase
Unbalance	9	3·6e-4 kg m	− 90°	0·225	9	3·25e-4 kg m	− 93·5°	− 10%	− 1·9%
Unbalance	35	3·6e-4 kg m	− 90°		35	3·68e-4 kg m	− 84·7°	2%	2·9%
			1400–1900 r.p.m						
				0·398	10	4·16e-4 kg m	− 77·7°	16%	6·8%
					35	3·7e-4 kg m	− 77·9°	3%	6·7%

obtained in the speed range between 1400 and 1900 r.p.m. where the identification of both faults is accurate in position, module and phase. In fact, this speed range is between the rotor critical speed and does not include higher speeds and lower speeds where the fitting of the model is not so accurate. So a good strategy, in this case, is to choose the rotating speeds one at time in the range 1400–1900 r.p.m. or a set of them in the same range.

An example of identification with a rotating speed of 1729 r.p.m. is reported in the residual map in Figure 42, and resumed in Table 6. The relative residual value is very good if one considers that we are dealing with experimental data and module and phase have very slight errors. The localization of the first fault on node 9 instead of 10 has to be considered

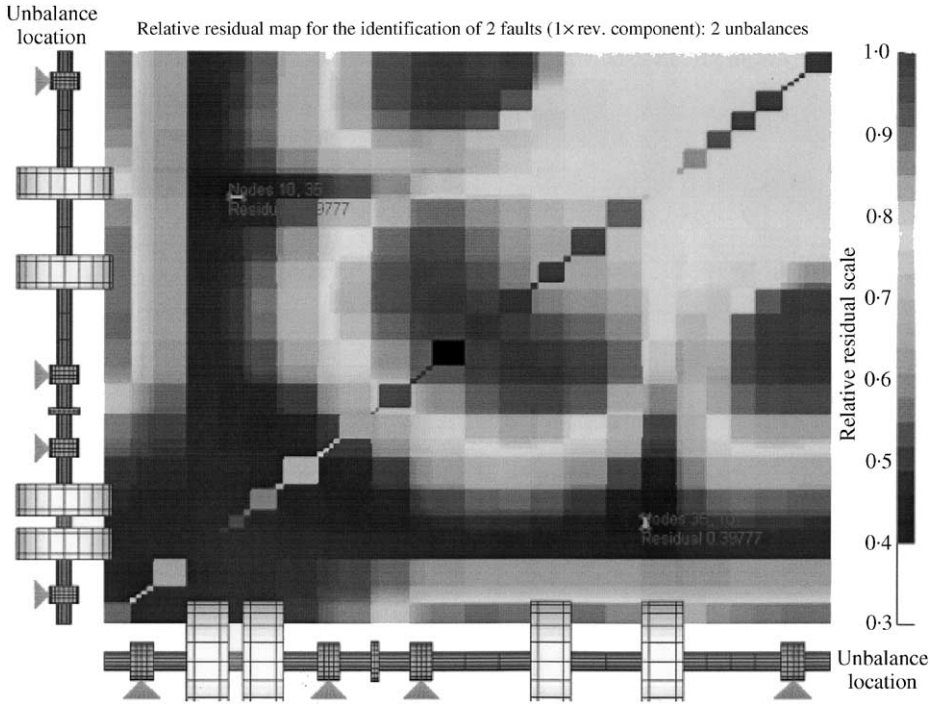

Figure 43. Residual map using the rotating speeds in the range 1400–1900 r.p.m.

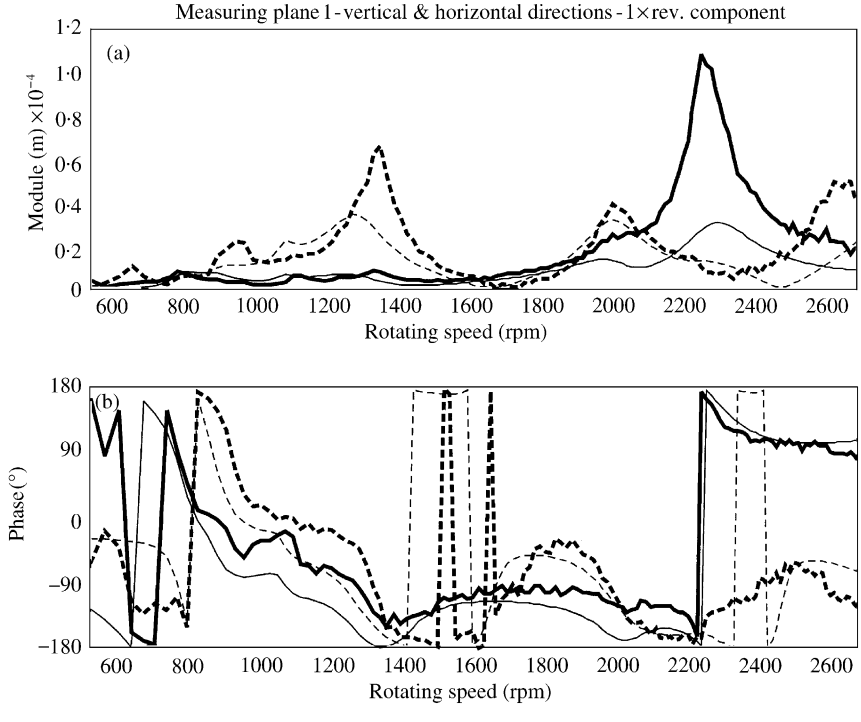

Figure 44. Comparison between experimental and analytical results using a rotating speed of 1729 r.p.m., bearing #1. —— Experimental vertical; — Analytical vertical; ■■■■ Experimental horizontal; – – – Analytical horizontal.

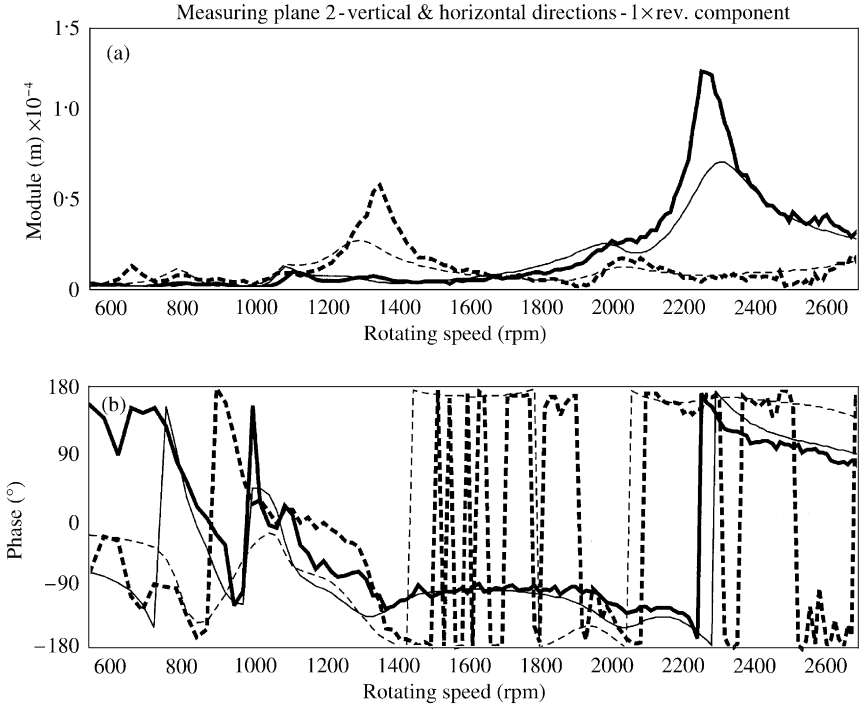

Figure 45. Comparison between experimental and analytical results using a rotating speed of 1729 r.p.m., bearing #2. —— Experimental vertical; — Analytical vertical; ■■■■ Experimental horizontal; – – – Analytical horizontal.

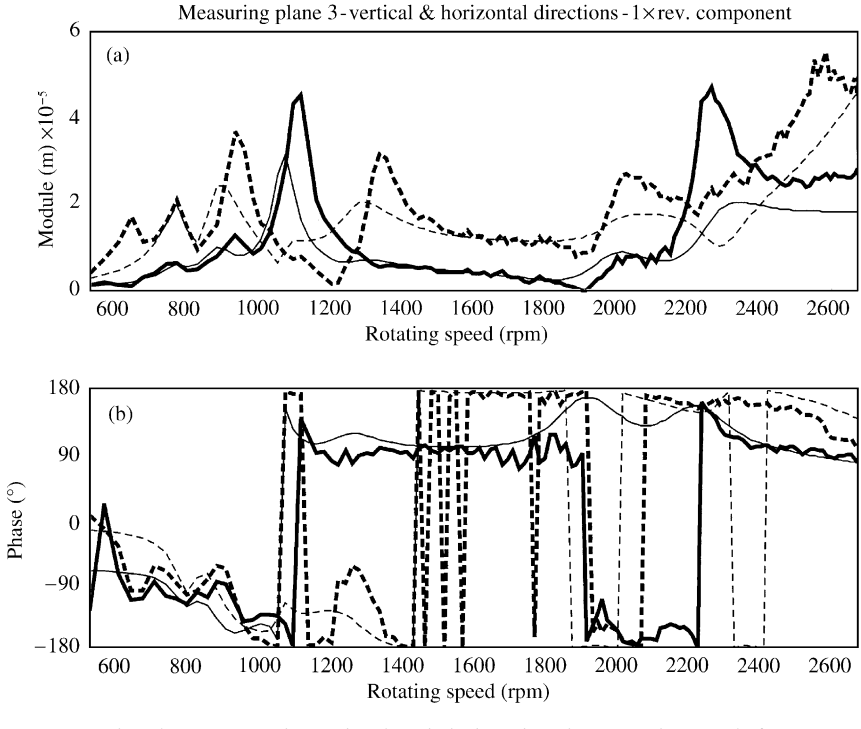

Figure 46. Comparison between experimental and analytical results using a rotating speed of 1729 r.p.m., bearing #3. —— Experimental vertical; — Analytical vertical; ■■■■ Experimental horizontal; – – – Analytical horizontal.

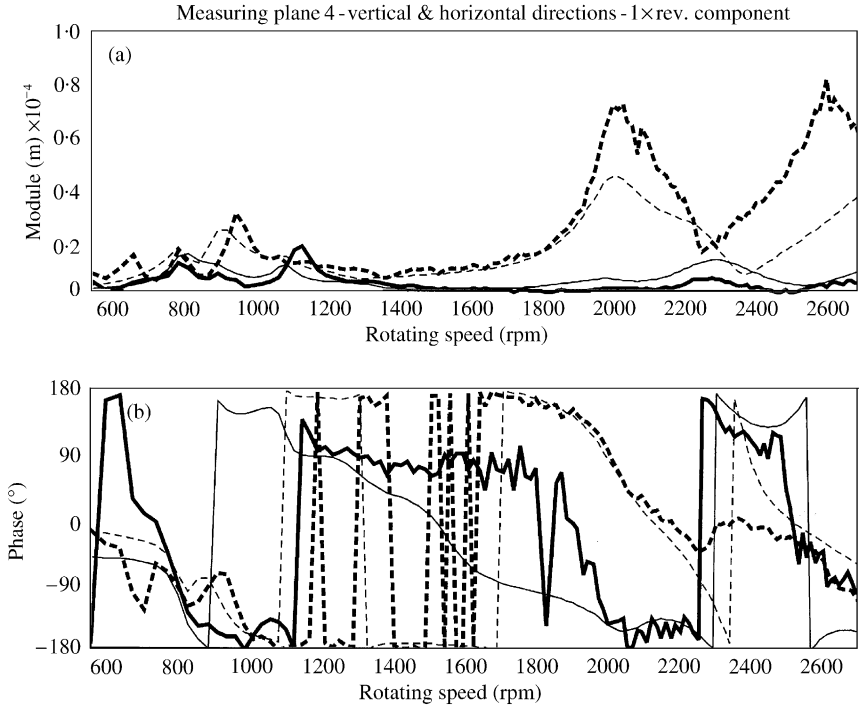

Figure 47. Comparison between experimental and analytical results using a rotating speed of 1729 r.p.m., bearing #4. —— Experimental vertical; — Analytical vertical; ■■■■ Experimental horizontal; – – – Analytical horizontal.

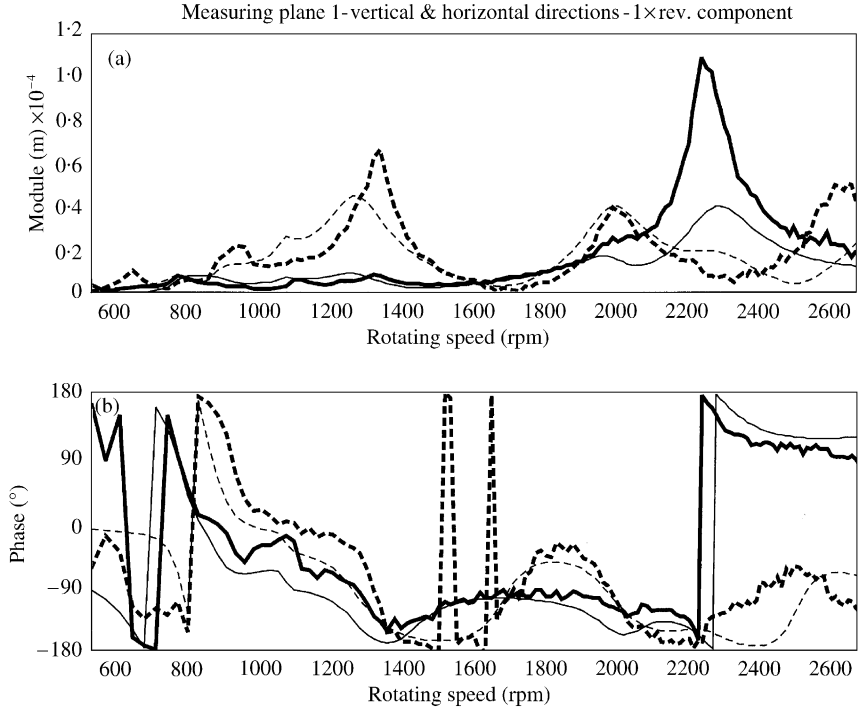

Figure 48. Comparison between experimental and analytical results using a rotating speed of 1400–1900 r.p.m., bearing #1. —— Experimental vertical; — Analytical vertical; ■■■■ Experimental horizontal; – – – Analytical horizontal.

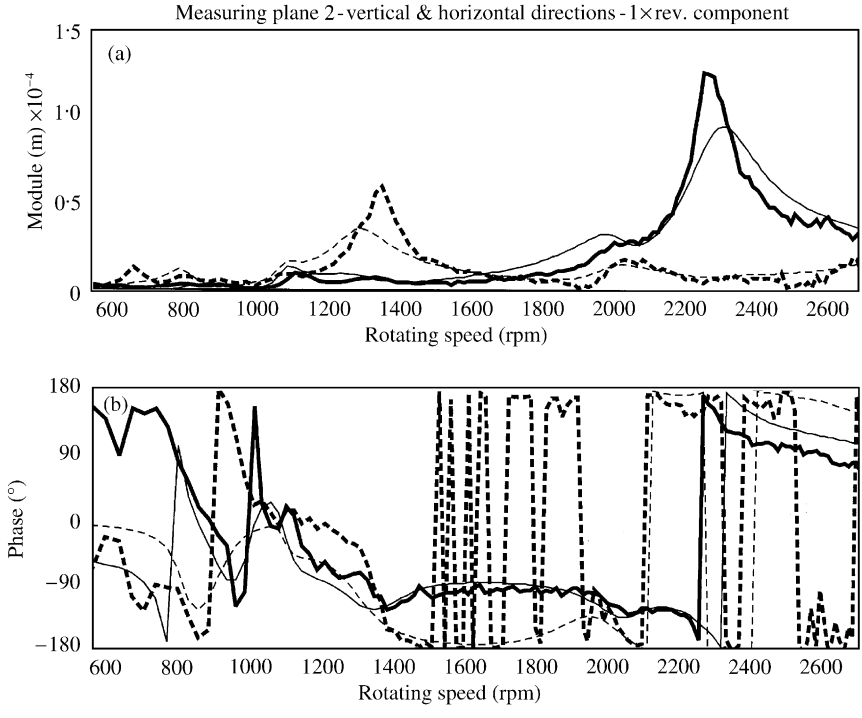

Figure 49. Comparison between experimental and analytical results using a rotating speed of 1400–1900 r.p.m., bearing #2. —— Experimental vertical; — Analytical vertical; ■■■■ Experimental horizontal; – – – Analytical horizontal.

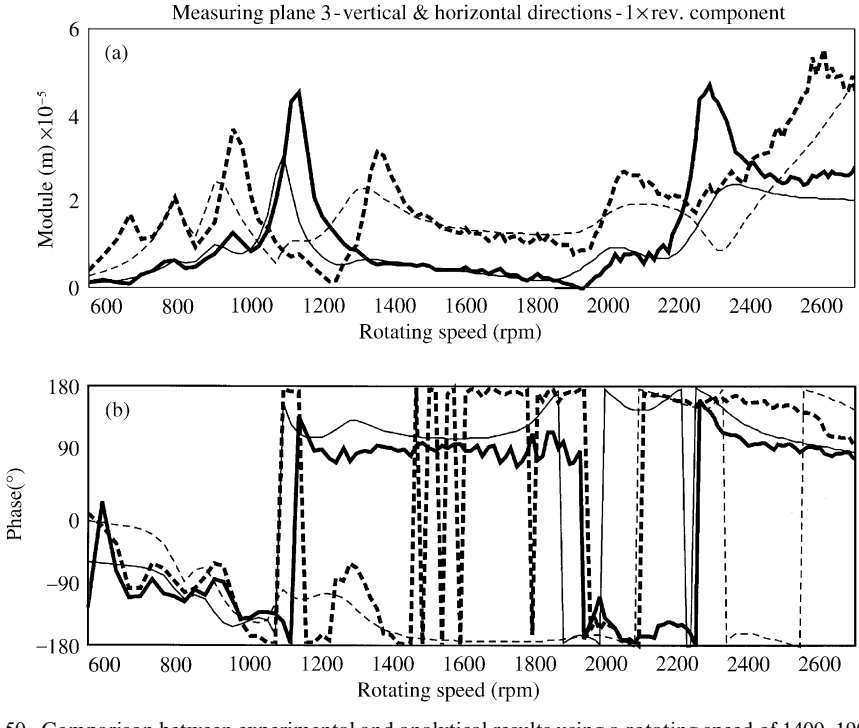

Figure 50. Comparison between experimental and analytical results using a rotating speed of 1400–1900 r.p.m., bearing #3. —— Experimental vertical; — Analytical vertical; ■■■■ Experimental horizontal; – – – Analytical horizontal.

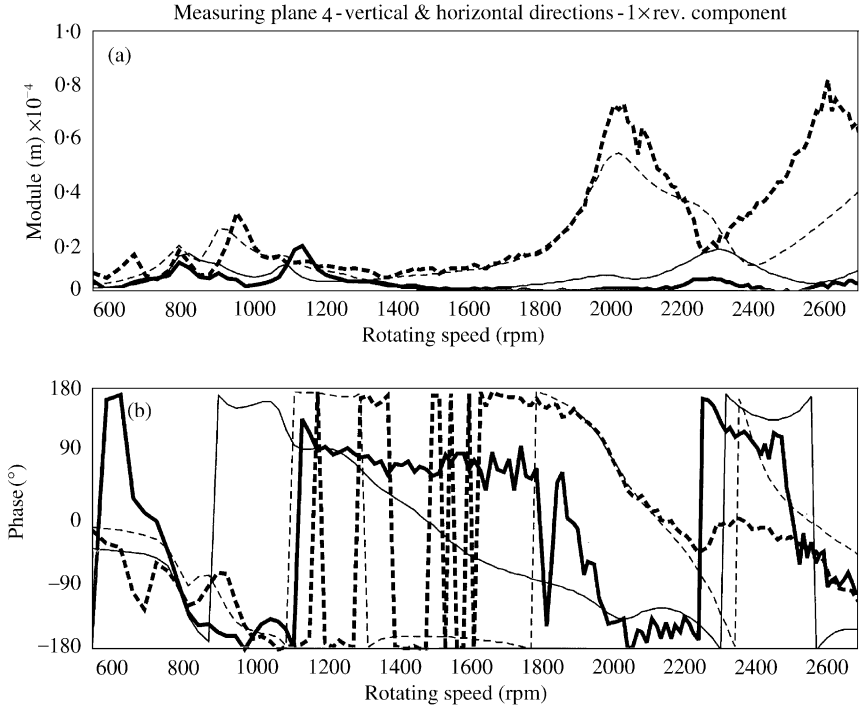

Figure 51. Comparison between experimental and analytical results using a rotating speed of 1400–1900 r.p.m., bearing #4. —— Experimental vertical; — Analytical vertical; ■■■■ Experimental horizontal; – – – Analytical horizontal.

by checking the f.e. model of the rotor (Figure 29), in which those nodes are very close to each other (20 mm).

The residual map obtained by using all the available rotating speeds between 1400 and 1900 r.p.m. is reported in Figure 43. Table 6 reports the identification results, which can be considered as good also in this case even if the relative residual value has increased and the module and phase of the faults have errors comparable to the case of the full speed range. However, the localization of the fault is correct.

If the results obtained by comparing the simulated results using the identified faults to the experimental measures, shown in Figures 44–51, are considered, the use of several rotating speeds allows to better reproduce the vibrational behaviour even if the relative residual is higher. Anyway, if also the results of the simulation in Figures 36–39, where all the available speed range was used, are considered, it can be seen that some aspects of the vibrational behaviour cannot be reproduced by the model. This consideration suggests, in field applications, when it is difficult to evaluate the validity range of the system models, the use of quality indexes of the identification that allow for including or excluding some rotating speeds from the identification procedure as described in reference [15].

6. CONCLUSIONS

A general method for the identification of multiple faults of different types is presented in this paper, by means of a model-based identification in the frequency domain. The models

of several types of faults are analyzed in detail. The method has been tested first on numerical simulations that have shown the effectiveness in identifying simultaneous faults of the same or different type, even on the same rotor of the shaft line. A special visualization aid, the residual map, has been introduced to make the localization of the faults and the evaluation of the identification correctness very quick and effective. Finally, a numerical validation has been performed in order to evaluate the robustness of the method with respect to modelling errors, represented by a random noise in the bearing coefficients. The results of this analysis have shown that the identification of both one and two simultaneous faults is rather robust with respect to modelling errors. Then, the method has been applied to experimental results obtained on a test-rig. Also in this case, the method proved to be effective in identifying the both faults in position, module and phase.

ACKNOWLEDGMENTS

This work is partially funded by the MURST (Italian Ministry for the University and Scientific Research) Cofinanziamento "Identificazione di Malfunzionamenti in Sistemi Meccanici" for the year 1999.

REFERENCES

1. R. ISERMANN 1995 2*nd International Symposium on Acoustical and Vibratory Surveillance Methods and Diagnostic Techniques*, *Senlis*, *France* 10–12 October 1995. Fault detection and diagnosis—methods and applications.
2. M. F. WHITE and M. JECMENICA 1999 12*th International Congress on Condition Monitoring and Diagnostic Engineering Management—COMADEM* 99, *Sunderland*, *U.K.*, July 1999. Fault diagnosis using a fault matrix incorporating fuzzy logic.
3. I. MAYES and J. E. T. PENNY 1999 12*th International Congress on Condition Monitoring and Diagnostic Engineering Management—COMADEM* 99, *Sunderland*. *U.K.*, July 1999. Model based diagnostics of faults in rotating machines.
4. T. KREUZINGER-JANIK and H. IRRETIER 2000 *IMechE—7th International Conference on Vibrations in Rotating Machinery*, *University of Nottingham*, *U.K.*, 12–14 September 2000, 335–346. Unbalance identification of flexible rotors based on experimental model analysis.
5. R. MARKERT, R. PLATZ and M. SIEDLER 2000 *ISROMAC—8 Conference*, *Honolulu*, *Hawaii*, 26–30 March 2000, 901–915. Model based fault identification in rotor systems by least squares fitting.
6. R. PLATZ, R. MARKERT and M. SEIDLER 2000 *IMechE—7th International Conference on Vibrations in Rotating Machinery*, *University of Nottingham*, *U.K.*, 12–14 September 2000, 581–590. Validation of online diagnostics of malfunctions in rotor systems.
7. S. EDWARDS, A. W. LEES and M. I. FRISWELL 2000 *IMechE—7th International Conference on Vibrations in Rotating Machinery*, *University of Nottingham*, *U.K.*, 12–14 September 2000, 323–334. Estimating rotor unbalance from a single run-down.
8 N. BACHSCHMID and P. PENNACCHI 2000 *IMechE—7th International Conference on Vibrations in Rotating Machinery*, *University of Nottingham*, *U.K.*, 12–14 September 2000, 571–580. Model based malfunction identification from bearing measurements.
9. N. BACHSCHMID, A. VANIA, E. TANZI and P. PENNACCHI 1999 *EURO DINAME* 99*—Dynamic Problems in Mechanics and Mechatronics*, *Wissenschaftszentrum Schloß Reisenburg der Universität Ulm*, *Günzburg*, *Germany*, 11–16 July 1999, 3–11. Identification and simulation of faults in rotor systems: experimental results.
10. N. BACHSCHMID, P. PENNACCHI, E. TANZI and A. VANIA 2000 *Journal of the Brazilian Society of Mechanical Sciences*, **XXII**, 423–442. Accuracy of modelling and identification of malfunctions in rotor systems: experimental results.
11. N. BACHSCHMID, P. PENNACCHI, E. TANZI and S. AUDEBERT 2000 *ISROMAC–8 Conference*, *Honolulu*, *Hawaii*, 26–30 March 2000, 1065–1072. Identification of transverse cracks in rotors systems.

12. N. BACHSCHMID, P. PENNACCHI and S. AUDEBERT 2000 *CONEM* 2000—*Congreso Nacional de Engenharia Mecànica. Natal*, *Rio Grande do Norte*, *Brasil*, August 7–11, 2000 (on CD-ROM). Some results in model based transverse crack identification in rotor systems.
13. N. BACHSCHMID, A. VANIA and S. AUDEBERT 2000 *ISROMAC*—8 *Conference*, *Honolulu*, *Hawaii*, 26–30 March 2000, 1057–1064. A comparison of different methods for transverse crack modelling in rotor systems.
14. R. PROVASI, G. A. ZANETTA and A. VANIA 2000 *Mechanical Systems and Signal Processing* **13**(3), 327–341. The extended Kalman filter in the frequency domain for the identification of mechanical structures excited by sinusoidal multiple inputs.
15. A. VANIA and P. PENNACCHI 2001 XV *Congresso AIMETA di Meccanica Teorica e Applicata*, *Taormina*, 26–29 September 2001 (on CD-ROM). Measures of accuracy of model based identification of faults in rotormachinery.

APPENDIX A: NOMENCLATURE

$\mathbf{A}^{(k)}$	complex vector of the kth fault
$\mathbf{D}$	damping matrix
$\mathrm{d}\mathbf{D}$	damping matrix change due to faults
$\mathrm{d}\mathbf{K}$	stiffness matrix change due to faults
$\mathrm{d}\mathbf{M}$	mass matrix change due to faults
$[\mathbf{E}(n\Omega)]$	system dynamical stiffness matrix
$\mathbf{F}$	force vector
$\mathbf{F}_f$	force vector due to faults
$\mathbf{F}_{fn}$	nth force vector harmonic component due to faults
$[\mathbf{F}_L^{(k)}]$	localization vector of the kth fault
F	force amplitude
$\mathbf{K}$	stiffness matrix
$\mathbf{M}$	moment vector, mass matrix
$\mathbf{M}_u$	original bow of the rotor
M	moment amplitude
m	number of faults, unbalance mass
n	number of the harmonic component
r	distance of the unbalance mass from the rotating axis
$\mathbf{U}$	original unbalance of the rotor
$\mathbf{W}$	rotor weight
$\mathbf{X}$	vector of vibration harmonic component
$\mathbf{X}_{\mathrm{A}n}$	partition of $\mathbf{X}_n$ for the nodes corresponding to measuring points
$\mathbf{X}_{\mathrm{B}n}$	partition of $\mathbf{X}_n$ for the nodes corresponding to measuring points
$\mathbf{X}_n$	nth vibration harmonic component
X_{st}	static deformation
$\mathbf{x}$	generalized displacement vector, vibration due to fault only
$\mathbf{x}_t$	rotor total vibration
$\mathbf{x}_1$	vibration due to weight original unbalance and bow
x	vertical node displacement
y	horizontal node displacement
z	rotor axial abscissa
$\boldsymbol{\alpha}_n$	inverse of $[\mathbf{E}(n\Omega)]$
$\boldsymbol{\alpha}_{\mathrm{B}n}$	partition of $\boldsymbol{\alpha}_n$ for the nodes corresponding to measuring points
$\boldsymbol{\alpha}_{\mathrm{A}n}$	partition of $\boldsymbol{\alpha}_n$ for the nodes not corresponding to measuring points
$\Delta\mathbf{x}^{(k)}$	kth radial misalignment in the coupling
$\Delta\phi^{(k)}$	kth angular misalignment in the coupling
$\Delta\mathbf{K}_n$	nth harmonic component in the stiffness Fourier expansion
$\boldsymbol{\delta}_n$	difference between calculated and measured vibrations
δ_{rn}	relative residual
ϑ_x	vertical node rotation
ϑ_y	horizontal node rotation
φ	phase
$\boldsymbol{\Omega}$	vector of rotating speeds
Ω	rotating speed, frequency